A CAR RNA FISH assay reveals functional and spatial heterogeneity of chimeric antigen receptor T cells in tissue

Karsten Eichholz[1], Alvason Zhenhua Li[1], Kurt Diem[2], Semih U. Tareen[3], Michael C. Jensen[4,5], Jia Zhu[1,2], Lawrence Corey[1,2,6*]

[1]Vaccine and Infectious Disease Division, Fred Hutchinson Cancer Research Center, Seattle, WA, USA.

[2]Department of Laboratory Medicine, University of Washington, Seattle, WA, USA.

[3]Work performed while employed at Juno Therapeutics, Seattle, WA; currently employed at Sana Biotechnology, Seattle, WA, USA.

[4]Clinical Research Division, Fred Hutchinson Cancer Research Center (FHCRC), Seattle, WA, USA.

[5]Ben Towne Center for Childhood Cancer Research, Seattle Children's Research Institute, Seattle, WA, USA.

[6]Department of Medicine, University of Washington, Seattle, WA, USA.

***correspondence**: L. Corey, MD, Fred Hutchinson Cancer Research Center, 1100 Fairview Ave N, MS E3-300, Seattle, WA 98190 (Lcorey@fredhutch.org).

One Sentence Summary: We developed a CAR RNA FISH assay to study chimeric antigen receptor T cell trafficking and function in human and mouse tissue.

Short title: A CAR RNA FISH assay to study CAR T cells in tissues

Abstract

Chimeric antigen receptor (CAR) T cells are engineered cells used in cancer therapy and are studied to treat infectious diseases. Trafficking and persistence of CAR T cells is an important requirement for efficacy to target cancer and HIV sanctuary sites. Here, we describe a CAR RNA FISH histocytometry platform combined with a dnnRRS image analysis algorithm to quantitate spatial distribution and in vivo functional ability of a CAR T cell population at a single cell resolution. In situ, CAR T cell exhibited a heterogenous effector gene expression and this was related to the distance from tumor cells, allowing a quantitative assessment of the potential in vivo effectiveness. The platform offers the potential to study immune functions engineered cells in situ with their target cells in tissues with high statistical power and thus, as an important tool for preclinical and potentially clinical assessment of CAR T cell effectiveness.

Impact statement

We developed an imaging platform and analysis pipeline to study large populations of engineered cells on a single cell level in situ.

39 **Introduction**

40 Chimeric antigen receptors (CAR) T cells are engineered T cells that are under development to
41 treat various cancers and infectious diseases. The CAR is a recombinant fusion protein that
42 combines an extracellular antigen-specific single chain variable fragment (scFv) with a membrane
43 domain and an intracellular signaling domain to promote targeted killing. The scFv is directed
44 against extracellular antigens, provides high specificity and induces cytolysis when the CAR T
45 cell interacts with its target. Recently, two CAR T cell therapies based on the anti-CD19 scFv
46 clone FMC63 have been approved for treatment of B-cell acute lymphoblastic leukemia (B-ALL)
47 and non-Hodgkin lymphoma and numerous constructs are in pre-clinical and clinical development
48 for a variety of hematological and solid tumors.

49 CAR T cell-based therapies are also in pre-clinical development to target the viral reservoir in
50 individuals infected with the human immune deficiency virus-1 (HIV-1) to provide a functional
51 cure. Anti-HIV CAR T cells either use a modified version of CD4, the cell surface protein
52 responsible for HIV attachment, or a scFv based on various HIV envelope protein gp120-specific
53 broadly-neutralizing antibodies, e.g. VRC01, VRC07-523, or PGT128*(1–3)*.

54 While CAR T cell therapies have shown some success in hematological cancers, the application
55 in solid tumors settings is still hampered by the immunosuppressive tumor microenvironment,
56 poor tumor infiltration, the choice of an efficient scFv-tumor antigen pair without off-target effects
57 and adverse effects like cytokine release syndrome*(4–6)*.

58 CAR T cell performance, proliferation and persistence in preclinical in vivo studies and clinical
59 application are mainly studied by flow cytometry, quantitative PCR, and for preclinical cancer
60 mouse models only, whole body bioluminescence imaging of the tumor burden. These techniques
61 are favorable to measure CAR T cell phenotype, functionality and expansion with high statistical

62 power and specificity and can assess global anti-tumor efficacy, however, the location of the CAR
63 T cells in the tissue with respect to the tumor cells cannot be determined.
64 To track CAR T cells by flow cytometry *in vitro* and *in situ,* various polypeptide tags like truncated
65 epidermal growth factor receptor (EGFRt) are co-expressed with the CAR*(7)*. These polypeptide
66 tags, like EGFRt, are not expressed on non-engineered T cells and show low immunogenicity.
67 EGFRt has been successfully used to study CAR T cells in vivo by flow cytometry in mice, humans
68 and nonhuman primates*(7–9)*, and the anti-EGFR mouse monoclonal antibody clone 31G7 has
69 been used to stain for CAR T cells in tissue *(7)*. However, to study CAR T cell trafficking and
70 function *in situ*, the use of anti-EGFRt antibodies is complicated by the ubiquitous expression of
71 EGFR in various healthy and tumor tissues as well as the limited possibility to multiplex different
72 target proteins available for fluorescence microscopy compared to multi-color flow cytometry. An
73 alternative technique is to use RNA *in situ* hybridization (RNA ISH) to track the CAR T cells.
74 Recently, RNA ISH approaches have been successfully applied to track CAR T cells in patients
75 with glioblastoma*(10)*, in a case study in a patient with B-ALL, who died 5 days post-anti-CD19
76 CAR T cell infusion*(11)* and in the clinical samples from the ZUMA-1 trial that tested the anti-
77 CD19 CAR Axicabtagene ciloleucel *(12)*.
78 Automated image analysis requires reliable image segmentation, however, commonly used
79 commercial and open source software mainly rely on nuclei detection and watershed algorithms.
80 The weak or discontinuous cell membrane staining, overlapping cells tissue- or fixation-derived
81 autofluorescence and other fluorescent artifacts have limited the use of current software packages
82 for automated image analysis. To overcome the limitations, stochastic algorithms that use hidden-
83 Markov-model (HMM) statistics proved to be useful to tackle the more advanced requirements of
84 automated image analysis in tissue *(13–17)*. More recently, we developed a robust and efficient

85 Random-Reaction-Seed method (RRS) that employs the maximum likelihood method to estimate
86 probabilistic functions of Markov chains which showed efficient tracking of neurite net-like
87 structures in fluorescence microscopy images *(18)*.
88 This article describes a dnnRRS-assisted RNA *in situ* hybridization assay to track and phenotype
89 tumor cells and anti-CD19 and anti-HIV envelope CAR T cells in tissues. We use this technique
90 to detect CAR T cells localization in tissue in a quantitative manner in both humans and preclinical
91 animal models. Our data indicate that proximity to tumor tissue influences in vivo killing potential
92 as defined by in situ IFNγ and GZMB mRNA expression; thus, providing direct in situ evidence
93 of in vivo activity and illustrating the importance of spatial interactions between the tumor
94 microenvironment and in vivo functional activity of adoptively transferred T cells The CAR RNA
95 FISH imaging platform can be easily modified for novel CAR-antigen pairs and the study of the
96 interactions between CAR T cell and the infiltrating tumor microenvironment and provide both
97 preclinical and clinical insights in determinants of potential CAR T cell effectiveness of this
98 emerging cellular therapy platform using commonly available technologies.

99

100 **Material and methods**

101 **Cell culture**

102 TM-LCL, Jurkat and VRC07-523 CAR Jurkat cells were cultured in RPMI1640 (Gibco), 10%
103 fetal bovine serum and antibiotics. The VRC07-523 CAR Jurkat cell line was a kind gift from
104 Hans-Peter Kiem.

105 **CAR T cells expansion**

106 Anti-CD19 CD8 CAR T cells were cultured with TM-LCL feeder cells as previously described
107 with minor modifications*(19)*. Briefly, 10^6 anti-CD19 CD8 CAR T cells were expanded in
108 presence of 7 x 10^6 irradiated (8000 cGy) TM-LCL feeder cells in RPMI1640 containing 50 IU/mL
109 human recombinant IL-2 (Peprotech), 10 ng/ml recombinant human lL-15 (Peprotech), 10% fetal
110 bovine serum, 50 µM β-mercaptoethanol (SigmaAldrich) and 25 mM Hepes, pH 7.4 (Gibco) and
111 antibiotics.

112 **Tissue samples**

113 The mouse tissues used for the CAR RNA FISH in situ validation contain a BE2 cell
114 neuroblastoma xenograft and were described in a previous study*(20)*.

115 **Flow cytometry**

116 Day 12 CD8 CAR T cells TM-LCL co-cultures were stained with LIVE/DEAD Fixable Aqua
117 Dead Cell Stain (ThermoFisher) followed by antibody staining against CD8 (FITC, clone RPA-
118 T8, BD, 555366), CD19 (BV786, clone SJ25C1, biolegend) and EGFRt (PE, clone erbitux,
119 provided by Juno Therapeutics) and analyzed on a LSR II flow cytometer. Gating on CD8+
120 EGFRt+ cells was done with fluorescence minus one-controls for CD8 and EGFRt.

121 **CAR RNA FISH – probes**

122 zz probes for CAR mRNA were custom-made by Acdbio and are directed against the scFv, the
123 signaling domain-coding region and in some cases the 3'UTR for CAR detection in tissues that

124 are devoid of any other lentiviral constructs that may harbor the wPRE (Fig. 1A, Fig. S1A). The
125 individual probes were compared *in silico* with the human, mouse and macaque (*M. mulatta* and
126 *M. nemestrina*) genome to avoid cross-detection of endogenous counterparts of the CAR (e.g.
127 CD3zeta).

128 **CAR RNA FISH sample preparation – cytospins**

129 To prepare cytospin slides to validate the probe specificity, 10^7 anti-CD19 CD8 CAR T cells or
130 Jurkat cells were washed twice with 40 mL PBS and centrifuged at 250 x g for 10 min. The cell
131 pellets were resuspended in 10 mL 4% paraformaldehyde, PBS, fixed at 37°C for 1 h, and washed
132 two times with 10 mL PBS. The cell pellet was then resuspended at 10^6 cell/mL in 70% ethanol
133 and stored for up to 7 days for further cytospin processing.

134 To obtain different densities of CAR T cells, CAR T cells were mixed with Jurkat cells at different
135 ratio (0 – 100%). The cell suspensions were then centrifuged onto RNAse-free Superfrost plus
136 glass slides (Electron microscopy sciences) with a cytospin centrifuge (cytospin 3,
137 ThermoShandon) set to 800 rpm for 10 min to prepare the cytospins.

138 The glass slides were air dried for 20 min at ambient temperature and dehydrated stepwise in 50%,
139 70% and absolute ethanol for 5 min and stored in absolute ethanol at -20ºC until further processing.

140 **CAR RNA FISH sample preparation – tissues**

141 Fresh frozen OCT-embedded tissues blocks were sectioned to 10 µm thickness onto RNAse-free
142 Superfrost plus glass slides (Electron microscopy sciences) on a Leica CM1950 cryostat at -20°C.
143 The slides were kept at -20°C for 1 h and transferred to -80°C or directly processed for FISH.

144 OCT sections were incubated in 4% PFA, PBS pre-chilled to 4°C for 15 min, washed 2 times
145 briefly with PBS and dehydrated in a graded series of ethanol for 5 min each (50%, 70%, 2 x
146 100%).

147 FFPE tissue blocks were sectioned to 4 µm thickness on a Leica RM2255 microtome. Sections
148 were heated at 60ºC for 1 h, dewaxed and processed for RNAscope pretreatment on a Leica Bond
149 RX according to manufacturer's recommendations with Leica Bond Epitope Retrieval Solution 2
150 (ACDbio) for 15 min at 95ºC. Subsequently, FFPE sections were processed manually as described
151 in the following section.

152 **Fluorescent CAR RNA FISH ISH procedure**

153 Cytospin slides or tissue section slides were removed from 100% ethanol after dehydration and
154 air-dried for 30 min at 40°C in a hybridization oven or 5 min at ambient temperature, respectively.
155 A hydrophobic barrier was created around the sample on the slides, air dried for 1 min, treated
156 with H_2O_2 for 10 min (for RNAscope® Multiplex Fluorescent Assay version 2) followed with
157 protease (30 min protease III at 40°C for cytospin samples, 15 min protease IV at ambient
158 temperature for mouse tissue sections in OCT-embedded tissues, or 30 min protease plus at 40°C
159 for FFPE tissues) (ACDbio).

160 After protease digestion, samples were washed twice in PBS and anti-RNA zz probes against CAR,
161 CD4, CD8, IFNγ, GZMB, PPIB and DapB were hybridized at 40°C for 2 h (Table 1 suppl.). As a
162 negative control, the slides were treated with 4 µg/mL RNAase A and 100 U/mL RNAse T1
163 (RNase A/T1 mix, ThermoFisher) for 30 min between the protease digestion and the probe
164 hybridization step. For the signal amplification after the probe hybridization, we used initially the
165 RNAscope Multiplex Fluorescent Assay version 1 with the fluorophores Alexa 488 and Atto 550
166 and in later experiments the RNAscope Multiplex Fluorescent Assay version 2 with the
167 fluorophores Opal 570 and Opal 650 (PerkinElmer) according the manufacturer's protocol for
168 multiplex fluorescent in situ hybridization kit with minor modifications. We added an additional
169 counter staining for the plasma membrane before the nuclear counter staining or omitted the

170 nuclear counterstaining completely. In brief, the sample slides were washed 2 times for 2 min with
171 PBS, incubated with 10 µg/mL wheat germ agglutinin conjugated with Texas Red-X or Oregon
172 Green 488 (Invitrogen) for 10 min at ambient temperature, washed again 2 times for 2 min with
173 PBS before proceeding to the nuclear counter staining step.

174 **Digital droplet PCR detection of CAR T cells in tissues**

175 gDNA and RNA were extracted with QiAmp DNA kit (Qiagen) and RNeasy Mini extraction kit
176 (Qiagen), respectively. 10 µL of DNA or RNA were used for ddPCR.
177 Primer sequences were as follows for wPRE (5′- CGCAACCCCCACTGGTT -3′ [wPRE forward],
178 5′-AAAGCGAAAGTCCCGGAAAG-3′ [wPRE reverse] and 5′- FAM-CCACCACCTGTCAGC-
179 MGB-3′ [wPRE probe]) and the CAR ORF (5′- AGCTGCCGATTTCCAGAAGA -3′ [CAR
180 forward], 5′- CCAGGTTCAGCTCGTTGTACAG -3′ [CAR reverse] and 5′- FAM-
181 TCAGCAGAAGCGCCGACGCC-QSY -3′ [CAR probe])
182 The DNA ddPCR was used with ddPCR Supermix for probe (Biorad) and the PCR conditions
183 were 95°C for 10 min, then 40 cycles at 94°C for 30 s, 60°C for 1 min followed by 98°C for
184 10min. The RNA-ddPCR was used with One-Step RT-ddPCR Advanced kit for Probes (Biorad).
185 The thermal conditions were 50°C for 60 min for reverse transcription, 95°C for 10 min, then 40
186 cycles at 94°C for 30 s, 60°C for 1 min for the ddPCR followed by 98°C for 10 min.

187 **Immunohistochemistry**

188 To combine IHC with the CAR RNA FISH procedure we followed a previously described protocol
189 with minor modification*(21)*. After the last RNA target was developed (step Amp4 in the
190 RNAscope Multiplex Fluorescent Assay version 1, TSA amplification step in the RNAscope
191 Multiplex Fluorescent Assay version 2), the cells and tissue sections were washed with PBS and
192 blocked with 5% donkey or goat serum (Jackson ImmunoResearch), 2% BSA (Gemini Bio-

193 Products) +0.2% Triton X-100 (SigmaAldrich) in 5X Casein (Vector Laboratories) for 30 min,
194 the mouse anti-huCD19 antibody (dilution 1:100,Clone ID: UMAB103, origene) overnight at 4°C
195 for the mouse xenograft tissues.
196 Slides were washed, incubated with secondary donkey anti-mouse IgG-Alexa 647 or Alexa 488
197 (1:100 Molecular Probes/ThermoFisher Scientific) or a goat anti-mouse BV480 (Becton
198 Dickinson) for 1 hour at room temperature, and washed 2 times for 5 minutes in PBS + tween
199 (0.05% v/v). Subsequently, samples were counterstained with DAPI and mounted with ProLong
200 Gold antifade (Thermofisher).

201 **Image acquisition**

202 Images were acquired with a PerkinElmer Ultraview Vox spinning disk confocal microscope
203 equipped with 4 laser lines 405, 488, 561 and 640 nm and a Hamamatsu ImageEM EMCCD
204 camera (512 x 512 pixels, 16 micron pixel size, 90% Quantum efficiency) with a 40 x objective, a
205 Leica SP8 confocal microscope equipped with laser lines at 405 nm, 440 nm, and adjustable white
206 light laser, or a Nikon eclipse Ti epifluorescence microscope equipped with a sola light machine,
207 a Hamamatsu ORCA-Flash4.0 LT+ C11440 (2048 ×2048 pixels, 82 % Quantum efficiency)
208 and Plan Apo 10x 0.45, Plan Apo 20x 0.75 and Plan Fluo 40x 1.3 objectives. Images that
209 were analyzed with dlRSS algorithm were not modified post-acquisition unless otherwise stated
210 in the description of the algorithm. Images for publication figures that were acquired with the
211 spinning disk confocal microscope were size-adjusted to 2048 x 2048 pixels and z-stacks were
212 projected with the Max intensity function in the Fiji software package*(22)*.
213 A Nikon Eclipse E800 with a Megapixel Nikon DigitalSight DS 5Mc color camera was used for
214 CAR in situ hybridization microscopy in human specimen.

215 **CAR T cell detection algorithm**

216 Imaging data was analyzed on a GPU workstation with a 32 core CPU, 64 GB RAM and a
217 QUADPRO P5000 GPU. To perform image segmentation based on WGA-plasma membrane
218 staining, we extended a previously described algorithm for identification of neurite net-like
219 structures and to generate the ground truth automatically for each image *(18)*. It is a robust and
220 efficient Random-Reaction-Seed method (RRS) that employs the maximum likelihood method to
221 estimate probabilistic functions of Markov chain. A U-net-based auto encoder decoder
222 convolutional deep neuronal network*(23)* performs image segmentation and phenotyping based on
223 the presence of nuclei, RNA and/or protein.
224 To detect the cell membrane two subsequent steps are performed by the algorithm. First, it extracts
225 a net-like draft of the cellular border based on the dnnRRS results and second, it performs cell-
226 loop segmentation of the net-like draft and thus, also removes false positive membranes from the
227 draft. Each tile of a tile scan is analyzed separately and to avoid any redundancy of areas that
228 overlap on the border of two adjacent images a 48-pixel wide area was omitted from the analysis
229 on each side of the tile. This equals to (4 x 48 x 2048 pixels)/(2048 x 2048 pixels) = 0.09 or 9% of
230 each slide that were not used for analysis. To overcome the optical vignetting effect in the corners
231 of the images were normalized using a Gaussian function.
232 For RNA FISH and CD19 IHC detection, a conventional local-maxima method is used and are
233 then combined with the membrane map. For the comparison of GZMB and IFNγ expression in
234 CAR T cells in the CD19high and CD19low areas, CD19high and CD19low areas were defined
235 by generating a circle for each CD19+ cells that corresponds to the actual area covered by the cell
236 at its x y position. The circles were than expanded approximately 16 times the radius of the circle
237 and connective groups were created by overlapping the expanded circles. The largest connective
238 group was denoted as CD19high area whereas the remainder of the tissue section was defined as

239 CD19low area. The spatial density of CAR+ GZMB-, CAR+ GZMB+, CAR+ IFNγ -, CAR+ IFNγ
240 + was than calculated for the CD19high and CD19low area of each individual tissue section.
241 The RNA and protein expression levels as well as the location of the cells was exported as a
242 comma-separated values file and loaded into the flow cytometry data analysis software FlowJo 10
243 (Becton Dickinson). In FlowJo, the imaging data was analyzed with the gating and plotting tools.
244 To compare cell counts of the dnnRRA and manual operators, manual operators used the cell
245 counter function in imageJ to track cell counts.

246 **Statistical analysis**

247 The data were analyzed with graphpad prism software with the statistical tests stated in the figure
248 legends. One-way ANOVA combined with a Tukey test was used to compare multiple groups. *,
249 **, ***, **** correspond to $p < 0.05$, $p < 0.01$, $p < 0.001$ and $p < 0.0001$, respectively. Paired t
250 test was used to compare the spatial density within the CD19high and CD19low areas. *, **, ***,
251 **** correspond to $p < 0.05$, $p < 0.01$, $p < 0.001$ and $p < 0.0001$, respectively.
252 Box and whiskers plots show the median, the 5th to 95th percentile for the whiskers and the 25th
253 to 75th percentile for the box.
254

255 **Results**

256 **Rationale for CAR RNA FISH probe design**

257 We designed the CAR RNA probes to be directed against the wPRE in the 3'UTR and the scFv of
258 the anti-CD19 CAR FMC63 and the anti-HIV env CAR VRC07-523 (Fig. 1A, Fig. 1A suppl.).
259 The scFv of the CAR is based on the variable region of the two mRNA species that translate to the
260 Ig heavy and light chain of an antibody. To rule out that the probes against the scFv cross-hybridize
261 with a large number of B cells in potential target tissues we stained human tonsil sections with a
262 pan-IGHG RNA FISH or a CAR FMC63 15ZZ probes. IGHG RNA FISH showed an ubiquitous
263 and bright staining throughout the tissue section (Fig. 2A suppl). By contrast, the CAR FMZ 63
264 15ZZ probes stained only a minority of cells in the tonsils tissue (Fig. 2B suppl. and inlet) and this
265 signal could be abrogated by RNAse pretreatment prior to CAR FMZ 63 15ZZ RNA FISH (Fig.
266 2C suppl.). We concluded that the number of B cells that stained false-positive for CAR FMZ 63
267 15ZZ RNA FISH was sufficiently small to optimize the CAR RNA FISH approach in combination
268 with various T cell markers for the anti-CD19 CAR based on the mouse monoclonal antibody
269 clone FMC63*(24)* and the anti-HIV envelope CAR based on the broadly-neutralizing antibodies
270 VRC07-523*(25)* and combined it with a recently published image segmentation and analysis
271 algorithm*(18)*.

272 **CAR RNA FISH detects CAR T cells in *in vitro* cultures**

273 For *in vitro* experiments, T cells were co-cultured with γ-irradiated CD19-expressing TM-LCL
274 lymphoblastoid cells for 12 days and purity was assessed by flow cytometry (~90%) (Fig. 3 suppl.).
275 To validate the CAR FMC63 26ZZ probes, anti-CD19 CD8 CAR T cells or Jurkat cells were
276 processed for cytospins and stained for CAR mRNA (Fig. 1B). The anti-CD19 CD8 CAR T cells
277 stained positive with the CAR FMC63 26ZZ probe set. By contrast, Jurkat cells stained with the
278 CAR FMC63 26ZZ probe set were negative for CAR RNA spots. RNA FISH against housekeeping

279 gene PPIB (Peptidyl-prolyl cis-trans isomerase B) and the bacterial gene DapB as positive and
280 negative controls, respectively, for RNA integrity and probe specificity, yielded characteristic
281 RNA FISH staining only in cells with relevant genes (Fig. 1B).
282 RNA FISH-based imaging techniques detect the target mRNA mostly in the cytosol that surrounds
283 the nucleus as demonstrated with the CAR mRNA (Fig. 4A suppl.). The density of tissue impedes
284 automated image segmentation to define the quantity of T cells expressing the majority of the
285 extranuclear CAR mRNA and cannot be defined based on the nuclear DAPI staining. Traditional
286 algorithms rely on nuclei detection and assume a slightly extended perimeter for the cytoplasm to
287 detect the RNA. To define cellular boundaries and to facilitate computational image segmentation,
288 we used fluorescently labeled wheat germ agglutinin as a second counterstain to label N-acetyl-D-
289 glucosamine and sialic acids on cell surface glycoproteins (Fig.1C). This allowed to analyze the
290 images with a modified version of a random reaction seed algorithm recently published by our
291 group *(18)* (Fig. 1D). In brief, the acquired images are partitioned and, several 1000 seeds are
292 distributed on the WGA plasma membrane stain images (Fig 1D). The algorithm searches for the
293 plasma membrane high fluorescence intensity signal, follows the signal using hidden Markov
294 model statistics and tries to close a loop, which would represent a cell and thus, creates a membrane
295 map*(18)*. Once the cell circumference has been determined, the algorithm uses classical Laplacian
296 of Gaussian local maxima detection for nuclear and RNA staining within this perimeter (Fig. 1D).
297 The output data contains the location and RNA expression levels of each individual cell of the
298 input image (Fig. 1D).
299 To validate the CAR RNA FISH approach in combination with the dnnRRS algorithm, we stained
300 anti-CD19 CD8 CAR T and Jurkat cells mixed at different ratio (1, 0.75, 0.5, 0.25 and 0) with the
301 CAR FMC63 26zz probe set and acquired images. The number of cells stained positive by CAR

302 RNA FISH and the number of cells detected with dnnRRS increased with incrementing number
303 of input anti-CD19 CD8 CAR T cells (Fig. 1E). The input CAR T cells were 90% EGFRt+ by
304 flow cytometry (Fig 1A suppl.), hence, we expected to detect ~ 90%, 67.5%, 45%, 22.5% and 0%
305 CAR+ cells for the corresponding ratio of 1, 0.75, 0.5, 0.25 and 0. The dnnRRS algorithm detected
306 ~5 – 60% CAR+ cells in the CD19 CAR T cell data set. There was a strong correlation between
307 detection of the algorithm and the expected values (R^2=0.95) (Fig. 1F) and a significantly higher
308 number of CAR RNA dots/cells compared to Jurkat cells alone (Fig. 1G). We chose the same
309 approach to validate CAR RNA FISH for a VRC07-523 CAR in a VRC07-523 CAR Jurkat cell
310 line and confirmed that it specifically stained these VRC07-523 CAR Jurkat cells but not control
311 Jurkat cells (Fig. 5A suppl.). In addition, in serial dilution experiments an increasing number of
312 cells stained positive for the VRC07-523 CAR RNA and this was detectable by dnnRRS (Fig. 5B
313 suppl.). The ratio of detected cells by dnnRRS (7- 68%) correlated with the expected values by
314 flow cytometry (0-97%) (R^2=0.98) (Fig. 5C suppl.) and we observed a significantly higher number
315 of CAR RNA dots/cell between the VRC07-523 CAR Jurkat cells at each ratio and non-transduced
316 Jurkat cells (Fig. 5D suppl.). Combined, these data indicate that our CAR RNA FISH probe design
317 and dnnRRS image analysis is highly specific and quantitative for detection of CAR T cells in cell
318 culture samples.

319 **CAR RNA FISH detect CAR T cells *in situ* in mouse xenografts**

320 To validate CAR RNA FISH for *in situ* applications in preclinical animal models, we used a BE2
321 neuroblastoma xenograft model of anti-CD19 CAR T cell-infused mice or control mice without
322 CAR T cell infusion*(20)*. The BE2 cell line was transduced with multiple lentiviruses to express
323 CD19 and luciferase and may contain the common wPRE sequence. We performed digital droplet
324 PCR with primers directed against the signaling domain and the wPRE in genomic DNA. We

325 detected the wPRE portion in both CAR+ and CAR- BE2 tumor tissue whereas the CAR signaling
326 domain was only present in CAR+ BE2 tumor tissues (Fig. 6 suppl.). Therefore, to exclude false-
327 positive cell detection due to cross-hybridization artifacts during the *in situ* setup of the CAR RNA
328 FISH on mouse xenograft tissues, we only used a reduced probe set of total 15 zz probes, coined
329 FMC63-15ZZ, and omitted the wPRE probes (Fig. 1A suppl.).
330 We observed a characteristic RNA FISH pattern with the CAR RNA FISH in CD19+ BE2
331 xenograft tissues from mice infused with anti-CD19 CAR T cells but not from control mice (Fig.
332 2A). To ensure that mRNA integrity was of sufficient quality in the mouse xenograft and the RNA
333 FISH staining procedure gave only low unspecific staining, we used probes against the house
334 keeping gene PPIB (Fig. 7A suppl.) and the bacterial gene DapB (Fig. 7B suppl.), which gave a
335 ubiquitous staining pattern or did not result in any positive signal in the corresponding area on
336 adjacent slides, respectively. To further confirm the specificity of the CAR RNA FISH signal, no
337 FISH signal could be observed when we omitted the FMC63 15ZZ probe set (Fig. 7C suppl.), or
338 after pretreatment of CAR T cell-positive tissues with RNAse A/H (Fig. 7D suppl.). These data
339 indicate that the CAR RNA FISH approach can be applied for CAR T cell detection in formalin
340 fixation and paraffin embedded tissues. We performed similar experiments in CAR T cell-positive
341 and -negative mouse xenograft tissue section that went through the process of fresh-frozen OCT
342 embedding and obtained similar results (data not shown).
343 To quantify the RNA expression of the CAR and any other mRNA of interest on a per cell basis
344 on the complete tissue section we used a novel and unique deep neuronal network random reaction
345 seed (dnnRRS) image analysis algorithm to perform computational image analysis *(18)*. WGA, a
346 lectin that binds N-acetyl-D-glucosamine and sialic acids on ubiquitous glycoproteins on the cell
347 surface allowed us to reliably define the cell boundaries of each cell in the tumor section (Fig. 2B).

348 The dnnRRS algorithm uses local fluorescence maxima detection for nuclei and RNA and random
349 reaction seed WGA-based image segmentation to quantify the spatial distribution and frequency
350 any mRNA of interest on a per cells and the data can be exported and analyzed in flow cytometry
351 analysis software like Flowjo by the individual researcher (Fig. 2C). To exemplify the performance
352 of the dnnRRS algorithm, we chose 10 images from our data set (Fig. 8A suppl.) that showed
353 typical fluorescence intensities for nuclei and membrane staining for different imaging situations.
354 Three operators counted the total cell number manually in imageJ based on membrane staining
355 and nuclei staining and the dnnRRS approach (Fig. 8B suppl.). The observed values obtained by
356 manual counting or dnnRRS correlated across the example images (Pearson's $r<0.9$ for each of
357 the operators) (Fig. 8C suppl.). The average time required per image was 15:31 min ± 8:02 min
358 for manual counting and 1:28 min ± 0:18 min for the dnnRRS algorithm (Fig. 8D suppl.). In
359 addition to the total number of cells, the dnnRRS algorithm also segments and quantifies RNA
360 FISH and IHC fluorescence data for T cell- or tumor-related genes, x-y position of the individual
361 cell and cellular borders and integrates and stitches adjacent micrograph images. Notably, the
362 image data sets recorded for the individual tissue sections frequently exceeded 300 multichannel
363 images per sections (data not shown) and we were thus able to interrogate multiplexed mRNA
364 expression levels in 150000 to 250000 cells per tissue section on a per cell basis.
365 We analyzed image data sets of a CAR RNA FISH or PPIB RNA FISH combined with
366 immunohistochemistry for CD19 from CAR T cell-positive and negative BE2 xenograft tissues
367 with the dnnRRS algorithm and used FlowJo for data analysis. We detected 32.6% and 0.13%
368 CAR+ in the CAR+ (Fig. 2D) and CAR- BE2 (Fig. 2E) tumor, respectively. CD19 expression was
369 below 1% and above 30% in CAR+ BE2 tumor and CAR- BE2 xenograft (Fig. 2D, E),
370 respectively. In the CAR- BE2 tumor, PPIB and CD19 expression showed homogenous

371 distribution (Fig. 2F). By contrast, the areas that stained positive for CD19 were almost devoid of
372 PPIB expression in the CAR+ BE2 tumor and showed signs of recent tissues disruption or lysis
373 (Fig. 3G).

374 The distribution of CAR T cells *in vivo* differed spatially, and a substantial number of cells were
375 negative by CAR RNA FISH and CD19IHC in CAR+ BE2 tumor sections. To better characterize
376 this heterogeneity of the tumor composition, we performed additional combinational RNA FISH
377 for the CAR, CD19 and CD171, another highly expressed protein in neuroblastomas and in the
378 BE2 neuroblastoma cell line *(20, 26)*. We found up to 38% CD171RNA+/CD19- and less than
379 0.01% CD171RNA+/CD19+ cells in the CAR+ BE2 tumor and in stark contrast ~75%
380 CD171RNA+/CD19+ in the CAR- BE2 tumor (data not shown).

381 These data indicated that the CAR RNA FISH detects specifically CAR T cells in tissues from
382 preclinical *in vivo* models and that the dnnRRS algorithm can be used to analyze CAR T cell
383 abundance, spatial distribution and efficacy.

384 **CD4 and CD8 CAR T cells are widely distributed in the tumor and display differential**
385 **functional and spatial gene expression**

386 To further characterize the functionality of the CAR T cells, we then set out to do combinations of
387 multiplex RNA FISH for the CAR, the T cell lineage marker CD4 and CD8α, as well as the effector
388 genes IFNγ and GZMB and analyzed the image data sets with the dnnRRS algorithm to phenotype
389 the tissue.

390 Independent CAR RNA FISH in combination with CD4 or CD8α showed that the CD4 and CD8
391 CAR T cells are evenly distributed within the CAR+ foci (Fig. 3A, B). We then subjected the
392 image data to computational analysis with the dnnRRS algorithm. For the CAR and CD8α RNA
393 FISH, 20.6% of the total cells were CAR+/CD8α+ and 19.9% CAR+/CD8- (presumably

394 CAR+/CD4+ T cells). For the CAR and CD4 RNA FISH, 17.2% of the total cells were
395 CAR+/CD4+ and 24.4% CAR+/CD4- (presumably CAR+/CD8+ T cells) (Fig 3C, D). Thus, in
396 this model the tissue-based distribution was relatively similar between the CD4+ and Cd8+ CAR
397 T cells.
398 To further characterize the functionality and heterogeneity of the CAR T cell pool within the
399 CAR+ BE2 tumor, we performed IHC for CD19, CAR RNA FISH combined with either GZMB
400 or IFNγ RNA FISH. CAR+ cells that express high levels of GZMB RNA (Fig. 4A) or IFNγ RNA
401 (Fig. 4B) can be observed by confocal microscopy close to the residual tumor. Concomitantly,
402 CAR+ cells that are located in areas with low or absence of CD19 expression only express low
403 levels of either GZMB or IFNγ RNA (Fig. 9 suppl. A and B). Whole-tissue tile scans of the CD19,
404 CAR RNA FISH co-staining with either GZMB RNA FISH (n=5) (Fig. 4C) or IFNγ RNA FISH
405 (n=5) (Fig. 4D) also indicated that the highest expression of GZMB and IFNγ is in close proximity
406 to the tumor. Examples images from this scan are also shown in the data supplement (Fig. 9 suppl.
407 C and D). The data sets were analyzed by dnnRRS and the x y position of CD19+ and CAR+
408 GZMB-/CAR+ GZMB+ (Fig. 4E and Fig. 10 suppl.) or CAR+ IFNγ-/CAR+ IFNγ+ (Fig. 5F and
409 Fig. 11 suppl.) cell were plotted separately or combined in Flowjo.
410 Around 2500 or 2800 CD19+ cells were detected in the GZMB and IFNγ datasets, respectively
411 (Fig. 5A). We detected approximately >31000 CAR+ GZMB- and 700 CAR+ GZMB+ cells/tissue
412 section as well as >36000 CAR+IFNγ- and 40 CAR+ IFNγ+ cells/tissue section (Fig. 5B).
413 Therefore, the frequency and spatial density of CAR+ GZMB+ was approximately 2% or 37
414 cells/mm2 whereas for CAR+IFNγ+ cells it was below 0.2% or 1.8 cells/mm2 (Fig. 5C, D). The
415 frequency and spatial density of CAR+ cells that were negative for either GZMB or IFNγ was
416 above 98% or around 1500 CAR+/mm2 (Fig. 5C, D).

417 We divided the spatial datasets in a CD19high and CD19low area to further analyze the effect of
418 tumor antigen expression on the spatial expression of the CAR T cell effector genes GZMB and
419 IFNγ (Fig. 5E). The spatial density of CD19+ cells/mm2 in the CD19high and CD19low area in
420 the GZMB and IFNγ dataset were significantly different (Fig. 5F, G) indicating that CAR T cells
421 had a higher probability for antigen exposure in the CD19high area. For the GZMB dataset, the
422 number of total CAR+ (Fig. 5H), CAR+ GZMB- (Fig. 5I) and CAR+GZMB+ cells/mm2 (Fig. 5J)
423 was not significantly different between the CD19high and CD19low area, however, there was a
424 trend towards higher spatial density of total CAR+ and CAR+ GZMB- cells/mm2 in the CD19low
425 area and an opposite trend of higher spatial density for CAR+GZMB+ cells/mm2 in the CD19high
426 area. The ratio of CAR+ GZMB+ to CAR+ GZMB- cells/mm2 was significantly higher in the
427 CD19high area (Fig. 6K). For the IFNγ dataset, the number of total CAR+ (Fig. 6L), CAR+ IFNγ-
428 (Fig. 6M) and CAR+ IFNγ+ cells/mm2 (Fig. 6N) was significantly higher in the CD19low area.
429 The ratio of CAR+ IFNγ+ to CAR+ IFNγ- cells/mm2 was not significant in a comparison of the
430 CD19high and CD19low area (Fig. 6O). In summary, these data indicate that the dnnRRS CAR
431 RNA FISH approach in combination with RNA FISH for T cell lineage and effector genes can
432 provide important insights into the spatial distribution and functionality of CAR T cells on a single
433 cell level and indicate that there is a high heterogeneity and differential spatial effector gene
434 expression in CAR T cells with respect to the tumor target cells.
435

436 **Discussion**

437 We describe here the development of a multiplex RNA FISH assay that is coupled with a dnnRRS
438 algorithm for image segmentation and quantitation. This assay allows to interrogate single cell
439 expression levels of multiple mRNA of interest and their spatial distribution and can be used to
440 detect, quantitate and evaluate the frequency and function of CAR T cells and cancer cells in
441 tissues. The use of specific probes directed against both the wPRE and scFv allows accurate
442 detection of CAR in tissues. It circumvents the common caveats of immunohistochemistry such
443 as long lead-time for antibody development and overlap of endogenous epitopes with the chimeric
444 protein of interest. This also allows to quickly modify this approach for *in situ* trafficking studies
445 for novel CARs with different target proteins, e.g. CD20, CD22, BMCA or any other genetically
446 modified cell *(27)* and can be used to study the interplay of CAR T cells, tumor cells and the tumor
447 microenvironment in solid tumor to develop novel strategies and hypothesis to improve CAR T
448 cell function in solid tumors; an area where CAR T cells therapies still fall short of the clinical
449 responses seen in hematologic cancers*(27, 28)*.
450 In the mouse xenograft samples, we identified 2 distinct CD19t-/CD171+ and CD19t+/CD171+
451 BE2 cell populations 7 days post-CAR T cells infusion. As our interest in this manuscript is
452 directed at using the probes to evaluate the structure intersecting between CAR T cells and tumor
453 tissue, we did not further investigate the underlying molecular mechanism in this artificial tumor
454 model because CD19 expression in this BE2-tumor model is driven from a lentiviral expression
455 cassette and the CD19+ BE2 cells in the xenograft sample were purified by magnetic bead
456 purification (Adam Johnson, Michael C. Jensen, personal communication). Interestingly, we
457 could not detect PPIB RNA (or other mRNA targets, data not shown) in the CD19+ areas that were
458 surrounded by IFNγ + and GZMB+ CAR T cells. While this may be merely a RNA preservation

459 problem in this specific area of the tissue specimen, global RNA degradation is also a hallmark of
460 apoptosis and the presence of IFNγ+ and GZMB+ CAR T cells in close proximity of the disrupted
461 PPIB-/CD19+ areas support the notion that they are indeed apoptotic.
462 Recently, the use of a defined CD4:CD8 ratio was implicated with synergistic antitumor effects
463 and better persistence *(29, 30)*. Our data indicate that CD4 and CD8 CAR T cells traffic into the
464 tumor site and probably undergo rapid proliferation. Not unexpectedly, the CD4 and CD8 CAR T
465 cells localize in close proximity of each other within the tumor at a ratio of ~1:1 at 7 days post-
466 infusion. This may indicate that the CD4 CAR T cells provide helper-function through secretion
467 of soluble factors. These observations suggest more detailed evaluation of samples using our
468 technology may provide insight into CAR T-cell responses and side effects.
469 The presence of CAR T cells expressing GZMB in close proximity at the border between the solid
470 tumor and adjacent tissue and the decreased expression in distant, CD19 negative tissues suggests
471 cell-to-cell contact with target cells is required for CAR T-cell activation. In contrast to the
472 GZMB+ CAR T cells, the more delocalized expression of IFNγ may indicate that these CAR T
473 cells migrate in and out from the area of the tumor surface more frequently or express IFNγ for an
474 extended period of time post-antigen exposure. Furthermore, there is still a considerable number
475 of CAR T cells close to the residual tumor surface that does not express IFNγ or GZMB and this
476 functional CAR T cell heterogeneity corroborate the findings of a *in vivo* live cell imaging study
477 by Cazaux and co-workers in which not every interaction of a CAR T cell with a tumor cell *in vivo*
478 led to CAR-mediated Ca^{2+}-signaling and killing *(31)*. However, a second study using a similar
479 approach by Mulazzani and Co-Workers did not report a heterogenous response after CAR T cell
480 infusion *(32)*. More recently, a third study by Chen and Co-workers reported an
481 immunohistochemistry and in situ hybridization approach and computational analysis of the anti-

482 CD19 CAR Axicabtagene ciloleucel in diffuse large B-cell lymphoma in the ZUMA-1 clinical
483 trial 5 days post-infusion *(12)*. Interestingly, less than 5% of the T cells were CAR T cells, in which
484 74% expressed IFNγ mRNA and 31% expressed GZMB protein whereas the number of bystander
485 CD3+ cells that expressed these markers exceeded the CAR T cells by 5-10 fold in absolute
486 numbers. The authors concluded that the non-CAR cells are the primary source of immune cell
487 activation and IFNγ production and their data indicate that there is also some degree of functional
488 heterogeneity of CAR T cells in a clinical setting. In our sample material bystander T cells and
489 other immune cells are absent and the frequency of GZMB+ and IFNγ + CAR T cells is
490 substantially lower 10 days post-infusion and warrants further studies into the contribution of
491 bystander immune cells and the suitability of tumor mouse models. Of note, an important
492 distinction between our study and the three studies is the costimulatory domain of the CAR. In our
493 sample tissue, a 41bb costimulatory domain was used whereas a CD28 costimulatory domain was
494 used in the two mouse studies and the study in clinical specimen*(12, 31, 32)*, which reportedly
495 have different kinetics and persistence in vivo. Further studies into CAR T cell functional
496 heterogeneity in xenograft models and human tumor and healthy tissue and how it relates to
497 clinical response rates will likely contribute to improvement of future CAR T cells interventions.
498 Methodically, the in vivo two photon microscopy assays published by Cazaux and Co-workers as
499 well as by Mulazzani and Co-Workers allow to study eGFP-expressing murine CAR T cells in
500 brain, lung, bone marrow and lymphoid tissue of xenografted mice *(31, 32)* and permit to perform
501 *in vivo* live tracking studies over days and weeks. These will be particularly helpful to better
502 understand the in vivo dynamics of CAR T cells in mice over time, however, the application of
503 two photon microscopy is still hampered in larger animal models and human because of the
504 limitations of deep tissue imaging and high immunogenicity of fluorescent proteins in immune-

505 competent large animal models and humans. The approach to phenotype CAR T cells in situ
506 reported by Chen and Coworkers is similar to ours in that it uses a computer algorithm to analyze
507 complex multicolor image datasets derived from tissue sections. Notable differences are that the
508 dnnRRS algorithm performs semi-supervised machine learning on whole tissue sections and does
509 the analysis of multicolor fluorescence IHC and FISH in the same run. Chen and coworkers report
510 a supervised analysis of 3-5 fields of view for the fluorescent IHC images and a separately analysis
511 for chromogenic RNA FISH*(12)*.
512 Globally, our studies provide insight on how CAR T cells are acting within in a solid tumor setting.
513 The IFNγ-expressing CAR T cells may change the local tumor microenvironment such as M2-to-
514 M1 macrophage differentiation or stimulate incoming tumor-infiltrating T cells and, thus gradually
515 lead to tumor regression. However, extended IFNγ-expression from tumor-infiltrating T
516 lymphocytes is associated with increase PD-1L expression and immune evasion in melanoma *(33)*
517 and neuroblastoma*(34)* and thus, extended IFNγ secretion from CAR T cells may be also
518 detrimental in a solid tumor setting. Of note, high levels of serum IFNγ are also implicated in an
519 increased risk of grade 3–5 neurotoxicity in anti-CD19 CAR T cell therapy*(11, 35)*. Further
520 evaluation of *in situ* cytokine-chemokine expression of CAR T cells in tissue is likely to lead to
521 increased understanding of the mechanism of CAR T cell tumor killing and toxicity.
522 Quantitative PCR, flow cytometry and bioluminescence imaging are the main tools to study CAR
523 T cells in vivo pre-clinical and, to some extent, clinical studies. Even though these assays allow
524 high sample throughput, macroscopic analysis of the tumor mass and/or provide high statistical
525 power for quantification, none of them assesses the spatial distribution CAR T cells and the
526 interplay of CAR T cells and their targets.

527 The dnnRRS CAR RNA FISH approach described here provides an easy-to-go tool kit for the
528 CAR T cells studies and promises to provide insights into the trafficking, persistence and
529 phenotype of CAR T cells in liquid and solid tumors in large animal models and human to better
530 understand the interplay between the tumor microenvironment and CAR T cell function.
531 With respect to the application of CAR T cells in the treatment of HIV, we also validated probes
532 to study anti-HIV CAR T cells in tissues. In this regard, CAR T cell trafficking into germinal
533 centers and other anatomic sites that harbors the HIV reservoir is considered to be crucial for a
534 long-term HIV remission *(21, 36, 37)* and the technique described here may provide valuable
535 insights to improve CAR T cell therapeutic approaches for HIV iteratively. Likewise, dnnRRS
536 FISH may also be applicable for infectious disease research with the advent of novel RNA and
537 DNA FISH assays to study persistence of HIV reservoirs in immune-privileged sites in tissues*(21,*
538 *38)* and the renewed interest in novel cell-based immunotherapies for HIV*(2, 3)*.
539

540 **Bibliography**

541 1. L. Liu, B. Patel, M. H. Ghanem, V. Bundoc, Z. Zheng, R. A. Morgan, S. A. Rosenberg, B.
542 Dey, E. A. Berger, Novel CD4-Based Bispecific Chimeric Antigen Receptor Designed for
543 Enhanced Anti-HIV Potency and Absence of HIV Entry Receptor Activity, *J. Virol.* **89**, 6685–
544 6694 (2015).
545 2. R. S. Leibman, M. W. Richardson, C. T. Ellebrecht, C. R. Maldini, J. A. Glover, A. J. Secreto,
546 I. Kulikovskaya, S. F. Lacey, S. R. Akkina, Y. Yi, F. Shaheen, J. Wang, K. A. Dufendach, M. C.
547 Holmes, R. G. Collman, A. S. Payne, J. L. Riley, Supraphysiologic control over HIV-1
548 replication mediated by CD8 T cells expressing a re-engineered CD4-based chimeric antigen
549 receptor, *PLoS Pathog.* **13**, 1–30 (2017).
550 3. M. Hale, T. Mesojednik, G. S. Romano Ibarra, J. Sahni, A. Bernard, K. Sommer, A. M.
551 Scharenberg, D. J. Rawlings, T. A. Wagner, Engineering HIV-Resistant, Anti-HIV Chimeric
552 Antigen Receptor T Cells, *Mol. Ther.* **25**, 570–579 (2017).
553 4. R. A. Morgan, J. C. Yang, M. Kitano, M. E. Dudley, C. M. Laurencot, S. A. Rosenberg, Case
554 report of a serious adverse event following the administration of T cells transduced with a
555 chimeric antigen receptor recognizing ERBB2, *Mol. Ther.* **18**, 843–851 (2010).
556 5. K. Watanabe, S. Kuramitsu, A. D. Posey, C. H. June, Expanding the therapeutic window for
557 CAR T cell therapy in solid tumors: The knowns and unknowns of CAR T cell biology, *Front.*
558 *Immunol.* **9**, 1–12 (2018).
559 6. M. R. Parkhurst, J. C. Yang, R. C. Langan, M. E. Dudley, D. A. N. Nathan, S. A. Feldman, J.
560 L. Davis, R. A. Morgan, M. J. Merino, R. M. Sherry, M. S. Hughes, U. S. Kammula, G. Q. Phan,
561 R. M. Lim, S. A. Wank, N. P. Restifo, P. F. Robbins, C. M. Laurencot, S. A. Rosenberg, T cells
562 targeting carcinoembryonic antigen can mediate regression of metastatic colorectal cancer but

563 induce severe transient colitis, *Mol. Ther.* **19**, 620–626 (2011).

564 7. X. Wang, W. C. Chang, C. L. W. Wong, D. Colcher, M. Sherman, J. R. Ostberg, S. J. Forman,
565 S. R. Riddell, M. C. Jensen, A transgene-encoded cell surface polypeptide for selection, in vivo
566 tracking, and ablation of engineered cells, *Blood* **118**, 1255–1263 (2011).

567 8. A. Taraseviciute, V. Tkachev, R. Ponce, C. J. Turtle, J. M. Snyder, H. D. Liggitt, D. Myerson,
568 L. Gonzalez-Cuyar, A. Baldessari, C. English, A. Yu, H. Zheng, S. N. Furlan, D. J. Hunt, V.
569 Hoglund, O. Finney, H. Brakke, B. R. Blazar, C. Berger, S. Riddell, R. Gardner, L. S. Kean, M.
570 C. Jensen, Chimeric Antigen Receptor T Cell-Mediated Neurotoxicity in Non-Human Primates,
571 *Cancer Discov.* **8**, 750–763 (2018).

572 9. C. J. Turtle, L. Hanafi, C. Berger, T. A. Gooley, S. Cherian, M. Hudecek, D. Sommermeyer,
573 K. Melville, B. Pender, T. M. Budiarto, E. Robinson, N. N. Steevens, C. Chaney, L. Soma, X.
574 Chen, C. Yeung, B. Wood, D. Li, J. Cao, S. Heimfeld, M. C. Jensen, S. R. Riddell, D. G.
575 Maloney, CD19 CAR – T cells of defined CD4+:CD8+ composition in adult B cell ALL
576 patients, *J Clin Invest* **1**, 1–16 (2016).

577 10. D. M. O'Rourke, M. P. Nasrallah, A. Desai, J. J. Melenhorst, K. Mansfield, J. J. D.
578 Morrissette, M. Martinez-Lage, S. Brem, E. Maloney, A. Shen, R. Isaacs, S. Mohan, G. Plesa, S.
579 F. Lacey, J. M. Navenot, Z. Zheng, B. L. Levine, H. Okada, C. H. June, J. L. Brogdon, M. V.
580 Maus, A single dose of peripherally infused EGFRvIII-directed CAR T cells mediates antigen
581 loss and induces adaptive resistance in patients with recurrent glioblastoma, *Sci. Transl. Med.* **9**,
582 eaaa0984 (2017).

583 11. A. E. Obstfeld, N. V. Frey, K. Mansfield, S. F. Lacey, C. H. June, D. L. Porter, J. J.
584 Melenhorst, M. A. Wasik, Cytokine release syndrome associated with chimeric-antigen receptor
585 T-cell therapy: clinicopathological insights, *Blood* **130**, 2569–2572 (2017).

586 12. P.-H. Chen, M. Lipschitz, J. L. Weirather, C. Jacobson, P. Armand, K. Wright, F. S. Hodi, Z.
587 J. Roberts, S. A. Sievers, J. Rossi, A. Bot, W. Y. Go, S. J. Rodig, Activation of CAR and non-
588 CAR T cells within the tumor microenvironment following CAR T-cell therapy, *JCI Insight* **5**
589 (2020).
590 13. L. E. Baum, T. Petrie, G. Soules, N. Weiss, A maximation techique occuring in the statistical
591 analysis of probablistic functions of markov chains, *Ann. Math. statisics* **41**, 164–171 (1970).
592 14. J. Li, A. Najmi, R. M. Gray, Image classification by a two-dimensional hidden Markov
593 model, *IEEE Trans. Signal Process.* **48**, 517–533 (2000).
594 15. R. Zhang, W. Ouyang, W. Cham, Image multi-scale edge detection using 3-D Hidden
595 Markov Model based on the non-decimated wavelet, *2009 16th IEEE Int. Conf. Image Process.*
596 *Cairo* , 2173–2176 (2009).
597 16. Y. Zhang, M. Brady, S. Smith, Segmentation of brain MR images through a hidden Markov
598 random field model and the expectation-maximization algorithm, *IEEE Trans. Med. Imaging* **20**,
599 45–47 (2001).
600 17. K. M. Kim, K. Son, G. T. R. Palmore, Neuron image analyzer: Automated and accurate
601 extraction of neuronal data from low quality images, *Sci. Rep.* **5**, 17062 (2015).
602 18. A. Li, L. Corey, J. Zhu, Random-reaction-seed method for automated identification of neurite
603 elongation and branching, *Sci. Rep.* **9**, 2908 (2019).
604 19. J. Wang, O. W. Press, C. G. Lindgren, P. Greenberg, S. Riddell, X. Qian, C. Laugen, A.
605 Raubitschek, S. J. Forman, M. C. Jensen, Cellular immunotherapy for follicular lymphoma using
606 genetically modified CD20-specific CD8+ cytotoxic T lymphocytes, *Mol. Ther.* **9**, 577–586
607 (2004).
608 20. A. Kunkele, A. J. Johnson, L. S. Rolczynski, C. A. Chang, V. Hoglund, K. S. Kelly-Spratt,

609 M. C. Jensen, Functional Tuning of CARs Reveals Signaling Threshold above Which CD8+
610 CTL Antitumor Potency Is Attenuated due to Cell Fas-FasL-Dependent AICD, *Cancer Immunol.*
611 *Res.* **3**, 368–379 (2015).
612 21. C. Deleage, S. W. Wietgrefe, G. Del Prete, D. R. Morcock, X.-P. Hao, M. Piatak, Jr., J. Bess,
613 J. L. Anderson, K. Perkey, C. Reilly, J. M. McCune, A. T. Haase, J. D. Lifson, T. W. Schacker,
614 J. D. Estes, Defining HIV and SIV Reservoirs in Lymphoid Tissues, *Pathog. Immun.* **1**, 68–106
615 (2016).
616 22. J. Schindelin, I. Arganda-Carreras, E. Frise, V. Kaynig, M. Longair, T. Pietzsch, S. Preibisch,
617 C. Rueden, S. Saalfeld, B. Schmid, J. Y. Tinevez, D. J. White, V. Hartenstein, K. Eliceiri, P.
618 Tomancak, A. Cardona, Fiji: An open-source platform for biological-image analysis, *Nat.*
619 *Methods* **9**, 676–682 (2012).
620 23. O. Ronneberger, P. Fischer, T. Brox, U-net: Convolutional networks for biomedical image
621 segmentation, *Lect. Notes Comput. Sci. (including Subser. Lect. Notes Artif. Intell. Lect. Notes*
622 *Bioinformatics)* **9351**, 234–241 (2015).
623 24. I. C. Nicholson, K. A. Lenton, D. J. Little, T. Decorso, F. T. Lee, A. M. Scott, H. Zola, A. W.
624 Hohmann, Construction and characterisation of a functional CD19 specific single chain Fv
625 fragment for immunotherapy of B lineage leukaemia and lymphoma, *Mol. Immunol.* **34**, 1157–
626 1165 (1997).
627 25. R. S. Rudicell, Y. D. Kwon, S.-Y. Ko, A. Pegu, M. K. Louder, I. S. Georgiev, X. Wu, J. Zhu,
628 J. C. Boyington, X. Chen, W. Shi, Z. -y. Yang, N. A. Doria-Rose, K. McKee, S. O'Dell, S. D.
629 Schmidt, G.-Y. Chuang, A. Druz, C. Soto, Y. Yang, B. Zhang, T. Zhou, J.-P. Todd, K. E. Lloyd,
630 J. Eudailey, K. E. Roberts, B. R. Donald, R. T. Bailer, J. Ledgerwood, J. C. Mullikin, L. Shapiro,
631 R. A. Koup, B. S. Graham, M. C. Nason, M. Connors, B. F. Haynes, S. S. Rao, M. Roederer, P.

632 D. Kwong, J. R. Mascola, G. J. Nabel, Enhanced Potency of a Broadly Neutralizing HIV-1
633 Antibody In Vitro Improves Protection against Lentiviral Infection In Vivo, *J. Virol.* **88**, 12669–
634 12682 (2014).
635 26. A. Taraseviciute, A. J. Johnson, M. C. Jensen, O. Finney, M. Berger, L. S. Finn, L. S.
636 Rolczynski, S. Mgebroff, A. Künkele, C. Brown, J. R. Park, C. Berger, C. A. Chang, Preclinical
637 Assessment of CD171-Directed CAR T-cell Adoptive Therapy for Childhood Neuroblastoma:
638 CE7 Epitope Target Safety and Product Manufacturing Feasibility, *Clin. Cancer Res.* **23**, 466–
639 477 (2016).
640 27. C. H. June, R. S. O'Connor, O. U. Kawalekar, S. Ghassemi, M. C. Milone, CAR T cell
641 immunotherapy for human cancer, *Science (80-.).* **359**, 1361–1365 (2018).
642 28. C. S. M. Yong, V. Dardalhon, C. Devaud, N. Taylor, P. K. Darcy, M. H. Kershaw, CAR T-
643 cell therapy of solid tumors, *Immunol. Cell Biol.* **95**, 356–363 (2017).
644 29. D. Sommermeyer, M. Hudecek, P. L. Kosasih, T. Gogishvili, D. G. Maloney, C. J. Turtle, S.
645 R. Riddell, Chimeric antigen receptor-modified T cells derived from de fi ned CD8+ and CD4+
646 subsets confer superior antitumor reactivity in vivo, *Leukemia* **30**, 492–500 (2016).
647 30. C. J. Turtle, L. Hanafi, C. Berger, M. Hudecek, B. Pender, E. Robinson, R. Hawkins, C.
648 Chaney, S. Cherian, X. Chen, L. Soma, B. Wood, D. Li, S. Heimfeld, S. R. Riddell, D. G.
649 Maloney, Immunotherapy of non-Hodgkin's lymphoma with a defined ratio of CD8+ and CD4+
650 CD19-specific chimeric antigen receptor – modified T cells, *Sci. Transl. Med.* **8**, 355ra116
651 (2016).
652 31. M. Cazaux, C. L. Grandjean, F. Lemaître, Z. Garcia, R. J. Beck, I. Milo, J. Postat, J. B.
653 Beltman, E. J. Cheadle, P. Bousso, Single-cell imaging of CAR T cell activity in vivo reveals
654 extensive functional and anatomical heterogeneity, *J. Exp. Med.* **216**, 1038–1049 (2019).

655 32. M. Mulazzani, S. P. Fräßle, I. von Mücke-Heim, S. Langer, X. Zhou, H. Ishikawa-
656 Ankerhold, J. Leube, W. Zhang, S. Dötsch, M. Svec, M. Rudelius, M. Dreyling, M. von
657 Bergwelt-Baildon, A. Straube, V. R. Buchholz, D. H. Busch, L. von Baumgarten, Long-term in
658 vivo microscopy of CAR T cell dynamics during eradication of CNS lymphoma in mice, *Proc.*
659 *Natl. Acad. Sci. U. S. A.* **116**, 24275–24284 (2019).
660 33. S. L. Topalian, J. M. Taube, A. P. Klein, R. A. Anders, D. M. Pardoll, S. Chen, H. Xu, T. L.
661 McMiller, L. Chen, R. Sharma, G. D. Young, Colocalization of Inflammatory Response with B7-
662 H1 Expression in Human Melanocytic Lesions Supports an Adaptive Resistance Mechanism of
663 Immune Escape, *Sci. Transl. Med.* **4**, 127ra37 (2012).
664 34. P. Srinivasan, X. Wu, M. Basu, C. Rossi, A. D. Sandler, PD-L1 checkpoint inhibition and
665 anti-CTLA-4 whole tumor cell vaccination counter adaptive immune resistance: A mouse
666 neuroblastoma model that mimics human disease, *PLoS Med.* **15**, e1002497 (2018).
667 35. J. Gust, K. A. Hay, L. A. Hanafi, D. Li, D. Myerson, L. F. Gonzalez-Cuyar, C. Yeung, W. C.
668 Liles, M. Wurfel, J. A. Lopez, J. Chen, D. Chung, S. Harju-Baker, T. Ozpolat, K. R. Fink, S. R.
669 Riddell, D. G. Maloney, C. J. Turtle, Endothelial activation and blood–brain barrier disruption in
670 neurotoxicity after adoptive immunotherapy with CD19 CAR-T cells, *Cancer Discov.* **7**, 1404–
671 1419 (2017).
672 36. K. P. Haran, A. Hajduczki, M. S. Pampusch, G. Mwakalundwa, D. A. Vargas-Inchaustegui,
673 E. G. Rakasz, E. Connick, E. A. Berger, P. J. Skinner, Simian immunodeficiency virus (SIV)-
674 specific chimeric antigen receptor-T cells engineered to target B cell follicles and suppress SIV
675 replication, *Front. Immunol.* **9**, 492 (2018).
676 37. V. I. Ayala, C. Deleage, M. T. Trivett, S. Jain, L. V. Coren, M. W. Breed, J. A. Kramer, J. A.
677 Thomas, J. D. Estes, J. D. Lifson, D. E. Ott, CXCR5-Dependent Entry of CD8 T Cells into

678 Rhesus Macaque B-Cell Follicles Achieved through T-Cell Engineering, *J. Virol.* **91**, e02507-16
679 (2017).
680 38. J. D. Estes, C. Kityo, F. Ssali, L. Swainson, K. N. Makamdop, G. Q. Del Prete, S. G. Deeks,
681 P. A. Luciw, J. G. Chipman, G. J. Beilman, T. Hoskuldsson, A. Khoruts, J. Anderson, C.
682 Deleage, J. Jasurda, T. E. Schmidt, M. Hafertepe, S. P. Callisto, H. Pearson, T. Reimann, J.
683 Schuster, J. Schoephoerster, P. Southern, K. Perkey, L. Shang, S. W. Wietgrefe, C. V. Fletcher,
684 J. D. Lifson, D. C. Douek, J. M. McCune, A. T. Haase, T. W. Schacker, Defining total-body
685 AIDS-virus burden with implications for curative strategies, *Nat. Med.* **23**, 1271–1276 (2017).
686
687

688 **Acknowledgements**

689 We thank S. Sun, L. Schroeder, P Guo, J. Vazquez and D. McDonald for technical support and
690 Mindy Miner for editing the manuscript. We thank Christopher W. Peterson and Hans-Peter Kiem
691 for providing the VRC07-523 CAR Jurkat cell line.

692 This independent research was supported by National Institute of Health grant UM1 A126623
693 and by the Gilead Sciences HIV Cure Grant Program.

694 This research was supported by the Experimental Histopathology Shared Resource of the Fred
695 Hutch/University of Washington Cancer Consortium (P30 CA015704).

696 This research was supported by the Cellular Imaging Shared Resource (CISR) of the Fred
697 Hutch/University of Washington Cancer Consortium (P30 CA015704).

698 SUT was a full-time employee of Juno Therapeutics during the period of performing this work.
699 The remaining authors declare no competing interest.

700 Code and data availability statement:

701 Code and raw data are available upon request

702 Author contributions:

703 K.E. and L.C. conceived the project. K.E. performed most experiments, analyzed the data
704 together with A.L. and interpreted the data together with LC.

705 A.L. developed the algorithm and A. L. and K.E. performed the dnnRRS analysis.

706 K.D. helped with experiments.

707 J.Z. helped with scientific advice and valuable expertise

708 S.T. designed the VRC07-523 CAR and provided scientific advice.

709 M.J. provided tissue samples and scientific advice.

710 KE and LC wrote the manuscript with input from all authors.

711 **Figures**

712 **Figure 1: CD19 CAR RNA FISH *in vitro* validation.**

713 The probes for CAR mRNA detection are directed against the scFv and wPRE and bridging areas
714 in the signaling domain of the CAR (A).

715 Cytospins of actively growing human anti-CD19 CD8 CAR T cells or Jurkat cells were stained
716 with CAR FMC63 26zz probes or PPIB (+ control) or DapB (- control) probes (B). CD19 CAR T
717 cells were stained with CAR FMC63 26zz probes-Alexa488 and Texas red-conjugated wheat germ
718 agglutinin to improve cell segmentation (C). dnnRRS analysis of multicolor raw images includes
719 nuclei and RNA detection as well random reaction seed detection of plasma membrane staining
720 (D). Fixed human anti-CD19 CD8 CAR T cells and Jurkat cells were mixed at different ratio,
721 processed for cytospins and stained with CAR FMC63 26zz probes-Atto550 and DAPI (E).
722 Correlation of CAR+ cells detected by dnnRRS analysis and flow cytometry (F). Comparison of
723 RNA dots/cells between different dilution steps. Statistics are calculated by one-way ANOVA
724 with Tukey's multiple comparison test (G). Staining experiments were performed at least 3 times
725 with technical duplicates.

726 Scale bar = 10 µm

727

728 **Figure 2: in situ detection of anti-CD19-CAR T cells in mouse xenografts of NSG mice after**
729 **anti-CD19 CAR T cell infusion.**

730 A BE2 neuroblastoma xenograft with ectopic expression of truncated CD19 and infused with anti-
731 CAR T cells or control T cells was used for the CAR RNA FISH *in situ* validation.

732 Staining of CAR+ and CAR- BE2 tumor tissue sections with CAR FMC63 15zz probes (red). The
733 red dotted line denotes an area that showed specific CAR RNA FISH staining (A). Staining of

734 CAR+ BE2 tumor with CAR FMC63 15zz probes and Texas Red-conjugated wheat germ
735 agglutinin improves cell segmentation (B). dnnRRS analysis of multicolor raw images includes
736 nuclei and CAR RNA detection as well random reaction seed detection of plasma membrane
737 staining. Data mining can be performed, and differential RNA expression and cell centers can be
738 visualized with Flowjo. The example picture derives from the area framed in white in B (C). A
739 thumbnail image and dnnRRS analysis of multiplex fluorescence RNA FISH and
740 immunohistochemistry staining of CAR RNA FISH and CD19 IHC (n=3) on CAR+ (D) and CAR-
741 (E) tumor sections shows the global CAR T cells distribution. A thumbnail image and dnnRRS
742 analysis of multiplex fluorescence RNA FISH and immunohistochemistry staining of PPIB RNA
743 FISH and CD19 IHC on CAR+ (F) and CAR- (G) tumor sections shows the global RNA integrity.
744

745 **Figure 3: CD4 and CD8 CAR T cells are present in the tumor and express IFNγ.**

746 CAR T cell lineage phenotyping was done with CAR RNA FISH in combination with CD4 and
747 CD8α, RNA FISH. A representative image are shown for CAR RNA and CD4 RNA (A) or CD8α
748 RNA (B) as well as nuclear and plasma membrane counterstaining. Thumbnail image of the
749 stitched multiplex fluorescence CAR (red) and CD4 (green) RNA FISH raw image channels and
750 dnnRRS analysis of a CAR+ BE2 tumor sections (n=3) (C). Thumbnail image of the stitched
751 multiplex fluorescence CAR (red) and CD8α (green) RNA FISH raw image channels and dnnRRS
752 analysis of a CAR+ BE2 tumor sections (n=3) (D).
753

754 **Figure 4: GZMB and IFNγ are highly expressed in a minority of CAR+ cells.**

755 CAR T cell functional phenotyping in a BE2 neuroblastoma xenograft was done by IHC for tumor
756 marker CD19 and CAR RNA FISH in combination with either GZMB (n=5) or IFNγ RNA FISH
757 (n=5). Confocal images of the combination of CAR RNA and CD19 with either GZMB RNA (A)

758 or IFNγ RNA in a representative area close to the residual tumor (B). The overview thumbnail
759 image of CAR RNA, CD19 with either GZMB RNA (C) or IFNγ RNA (D) staining shows the
760 global distribution of the different markers. dnnRRS analysis of the whole tissue section and the
761 various plots depict the spatial distribution of CD19+, CAR+ and GZMB+ (E) cells or IFNγ+ cells
762 (F). Scale bar = 10 µm
763
764 **Figure 5: Spatial density analysis of the GZMB+ and IFNγ+ CAR T cells in CD19high and**
765 **low areas reveals differential spatial effector gene expression**
766 Statistics of the CD19/CAR/GZMB (n=5) and CD19/CAR/IFNγ (n=5) cumulative datasets from
767 Figure 6 and supplementary Fig. 11 and 12. Total CD19+ cells/mm2 (A) as well as total (B),
768 frequency (C) and spatial density (D) of CAR+ GZMB-, CAR+ GZMB+, CAR+ IFNγ-, CAR+
769 IFNγ + are shown. An example shows how tissue sections were separated in CD19high and
770 CD19low areas denoted by the yellow color and, in this case the CAR+GZMB- cells as red dots
771 (E). Spatial density of CD19+ cells in the respective areas in the CD19/CAR/GZMB (n=5) (F) and
772 CD19/CAR/IFNγ (n=4) (G) cumulative datasets. In the CD19/CAR/GZMB cumulative dataset,
773 total CAR+ cells/mm2 (H), CAR+ GZMB- cells/mm2 (I), CAR+ GZMB+ cells/mm2 (J), ratio of
774 CAR+ GZMB+ to CAR+ GZMB- cells/mm2 (K) in the CD19high and CD19low area. In the
775 CD19/CAR/ IFNγ cumulative dataset, total CAR+ cells/mm2 (L), CAR+ IFNγ- cells/mm2 (M),
776 CAR+ IFNγ+ cells/mm2 (N), ratio of CAR+ IFNγ+ to CAR+ IFNγ- cells/mm2 (O) in the
777 CD19high and CD19low area. C-D were analyzed by one-way ANOVA. F-O were analyzed by
778 paired t test.
779
780 **Supplementary Figure 1: CAR probe table, principle of RNA FISH.**

781 Four zz probes sets were designed for detection of anti-CD19 and anti-HIV CAR T cells. The
782 probes bind to regions unique to the CAR mRNA that cannot be found in non-genetically
783 engineered organisms (A).
784
785 **Supplementary Figure 2: CAR FMC63-15zz probes on human tonsil tissue**
786 Human tonsil sections were stained for IGHG gene (A) or with FMC63-15zz probe with (B) or
787 without (C) RNAase pretreatment (n=2).
788 Scale bar = 1000 micrometers
789
790 **Supplementary Figure 3: purity of primary CAR T cell culture after expansion.**
791 Anti-CD19 CD8 CAR T cells were cultured with γ-irradiated CD19+ TM-LCL cells to stimulate
792 expansion. On day 12 of cell culture, CAR T cell purity was assessed by flow cytometry for the
793 cell surface markers CD19-BV786, EGFRt-PE and CD8-FITC (n=1). These cells were processed
794 for CAR RNA FISH and used for the *in vitro* validation.
795
796 **Supplementary Figure 4: CAR RNA FISH detects CAR RNA mainly extranuclear.**
797 VRC07-523 CAR Jurkat cells were stained with CAR VRC07-523 42zz probes and nuclear
798 counterstain to exemplify subcellular localization of CAR RNA. The CAR RNA is mainly detected
799 extranuclear or on the outline of the nuclear counterstain.
800
801 **Supplementary Figure 5: VRC07 CAR RNA FISH *in vitro* validation.**
802 Cytospins of VRC07-523 CAR-expressing Jurkat cells or non-transduced Jurkat cells were stained
803 with VRC07-523 42zz probes (A). Fixed human VRC07-523 CAR-expressing Jurkat cells and
804 non-transduced Jurkat cells were mixed at different ratio, processed for cytospins and stained with

805 VRC07-523 42zz probes and DAPI (B). Correlation of dnnRRS algorithm detected CAR+ cells
806 stained with the VRC07 42zz probes with expected ratio based on EGFRt+-flow cytometry (C).
807 Comparison of RNA dots/cells between different dilution steps. Statistics are calculated by one-
808 way ANOVA with Tukey's multiple comparison VRC07-523 CAR Jurkat data set (D).
809 Staining experiments were performed 3 times with technical duplicates.
810 Scale bar = 10 µm
811
812 **Supplementary Figure 6: presence and expression of CAR sequence and wPRE in mouse**
813 **xenografts.**
814 ddPCR analysis for the presence of the CAR signaling domain (CD8CD3) and the 3'UTR
815 containing the wPRE sequence of genomic DNA in xenograft tissue section from CAR T cell-
816 infused and control mice . (n=2). ddPCR primers and probes were directed against the CD3 CD8
817 region and wPRE portion to test for CAR and CD19 lentivirus-derived expression cassettes.
818
819 **Supplementary Figure 7: CAR RNA FISH in situ validation.**
820 Specificity of CAR RNA FISH in situ staining was further validated with RNA FISH staining for
821 housekeeping gene PPIB (A) and bacterial gene DapB (B) CAR RNA FISH protocol without the
822 addition of CAR FMZ63 15zz probes (C) or after RNAse treatment (D) (n=3).
823

824 **Supplementary Figure 8: Manual and dnnRRS cell counting numbers correlate with each**
825 **other**

826 We chose 10 images from the CAR+ BE2 tumor dataset that are exemplary for images without
827 artifacts or that show different imaging artifacts like strong membrane staining or weak nuclei
828 staining (A). Total cell numbers were counted manually by three operators or with the dnnRRS
829 algorithm using the nuclei and membrane WGA staining (B). Correlation of the number of cells
830 counted/images by the three operators and the dnnRRS method (C). The counting time
831 required/image is shown in (D).

832

833 **Supplementary Figure 9: Low effector gene expression in CAR T cells that located further**
834 **away from the tumor.**

835 CAR T cell functional phenotyping in a BE2 neuroblastoma xenograft was done by IHC for tumor
836 marker CD19 and CAR RNA FISH in combination with either GZMB (n=5) or IFNγ RNA FISH
837 (n=5). Confocal images of the combination of CAR RNA and CD19 with either GZMB RNA (A)
838 or IFNγ RNA (B) in a representative area far from the residual tumor. Exemplary wide field images
839 that were used to create the overview thumbnail images in Figure 5 image of CAR RNA, CD19
840 with either GZMB RNA (C) or IFNγ RNA (D).

841

842 **Supplementary Figure 10: dnnRRS analysis CD19, CAR and GZMB expression of tissue**
843 **sections from a BE2 tumor.**

844 CAR T cell functional phenotyping in a BE2 neuroblastoma xenograft was done by IHC for
845 tumor marker CD19 and CAR RNA FISH in combination with GZMB RNA FISH(n=4).

846 **Supplementary Figure 11: dnnRRS analysis CD19, CAR and IFNγ expression of tissue**

847 **sections from a BE2 tumor.**

848 CAR T cell functional phenotyping in a BE2 neuroblastoma xenograft was done by IHC for

849 tumor marker CD19 and CAR RNA FISH in combination with IFNγ RNA FISH (n=4).

850

851 **Supplementary Table 1: CAR RNA FISH probes and respective catalog number.**

Probe name	Catalog Number
VRC07-CAR-wPRE-O1	300031
FMC63 15ZZ	515321
FMC63 26ZZ	513551
FMC63 29ZZ	exclusive probe
DapB-C1	310043
Hs-PPIB-C2	313901-C2
Hs-PPIB-C1	313901-C1
Hs-GZMB	445971
Hs-GZMB-C2	445971-C2
Hs-CD8A-C3	560391-C3
Hs-CD4-C2	605601-C2
Hs- IFNγ-C1	310501-C1
Hs- IFNγ-C2	310501-C2

852

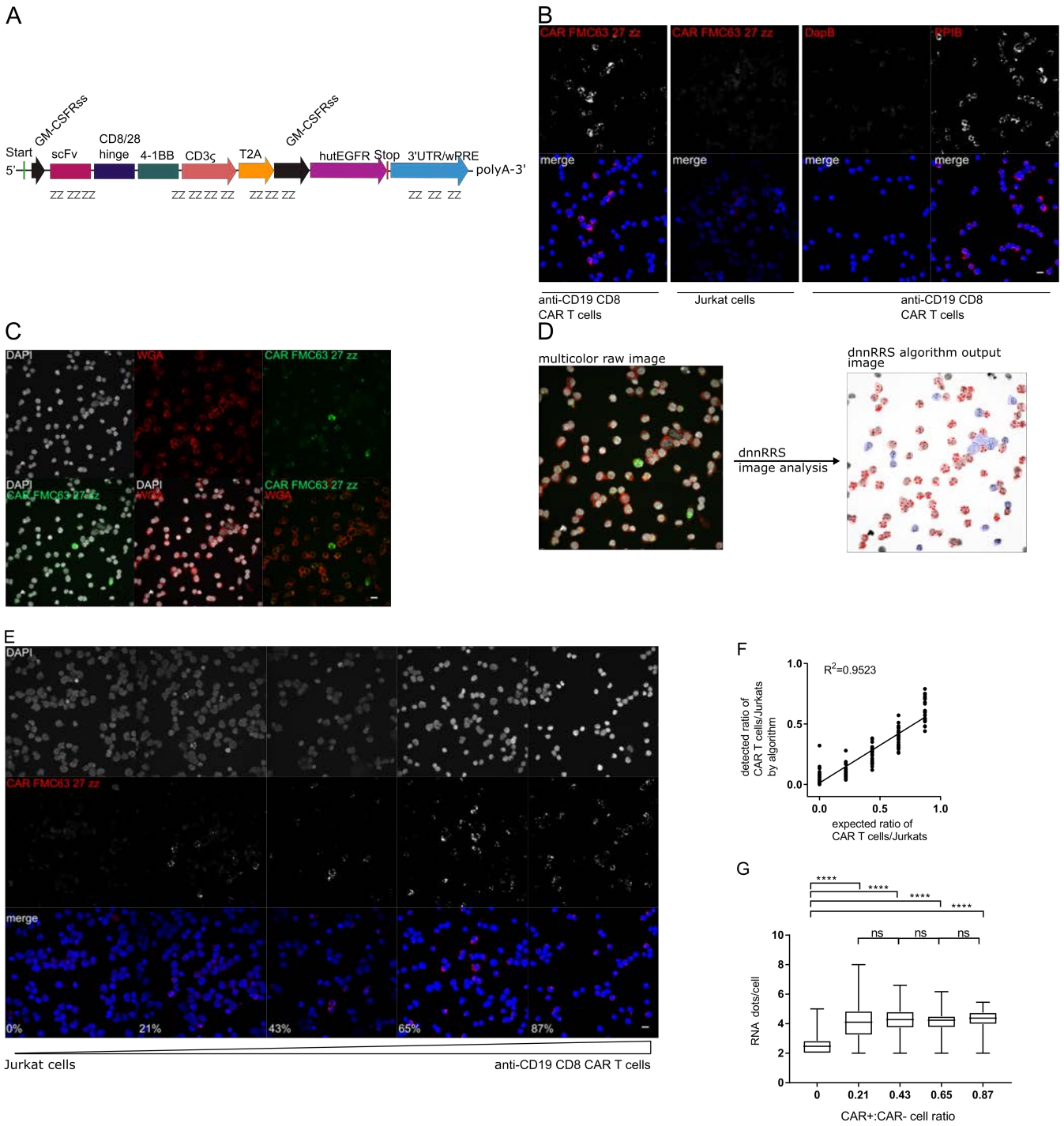
A
Start
5'
GM-CSFRss
scFv
CD8/28
hinge
4-1BB
CD3ζ
T2A
GM-CSFRss
hutEGFR Stop
3'UTR/wPRE
polyA-3'
B
CAR FMC63 27 zz
CAR FMC63 27 zz
DapB
SPIB
merge
merge
merge
merge
anti-CD19 CD8
CAR T cells
Jurkat cells
anti-CD19 CD8
CAR T cells
C
DAPI
WGA
CAR FMC63 27 zz
DAPI
CAR FMC63 27 zz
DAPI
WGA
CAR FMC63 27 zz
WGA
D
multicolor raw image
dnnRRS
image analysis
dnnRRS algorithm output
image
E
DAPI
CAR FMC63 27 zz
merge
0%
21%
43%
65%
87%
Jurkat cells
anti-CD19 CD8 CAR T cells
F
R2=0.9523
detected ratio of
CAR T cells/Jurkats
by algorithm
expected ratio of
CAR T cells/Jurkats
G
****
****
****
****
ns
ns
ns
RNA dots/cell
CAR+:CAR- cell ratio

Figure 1

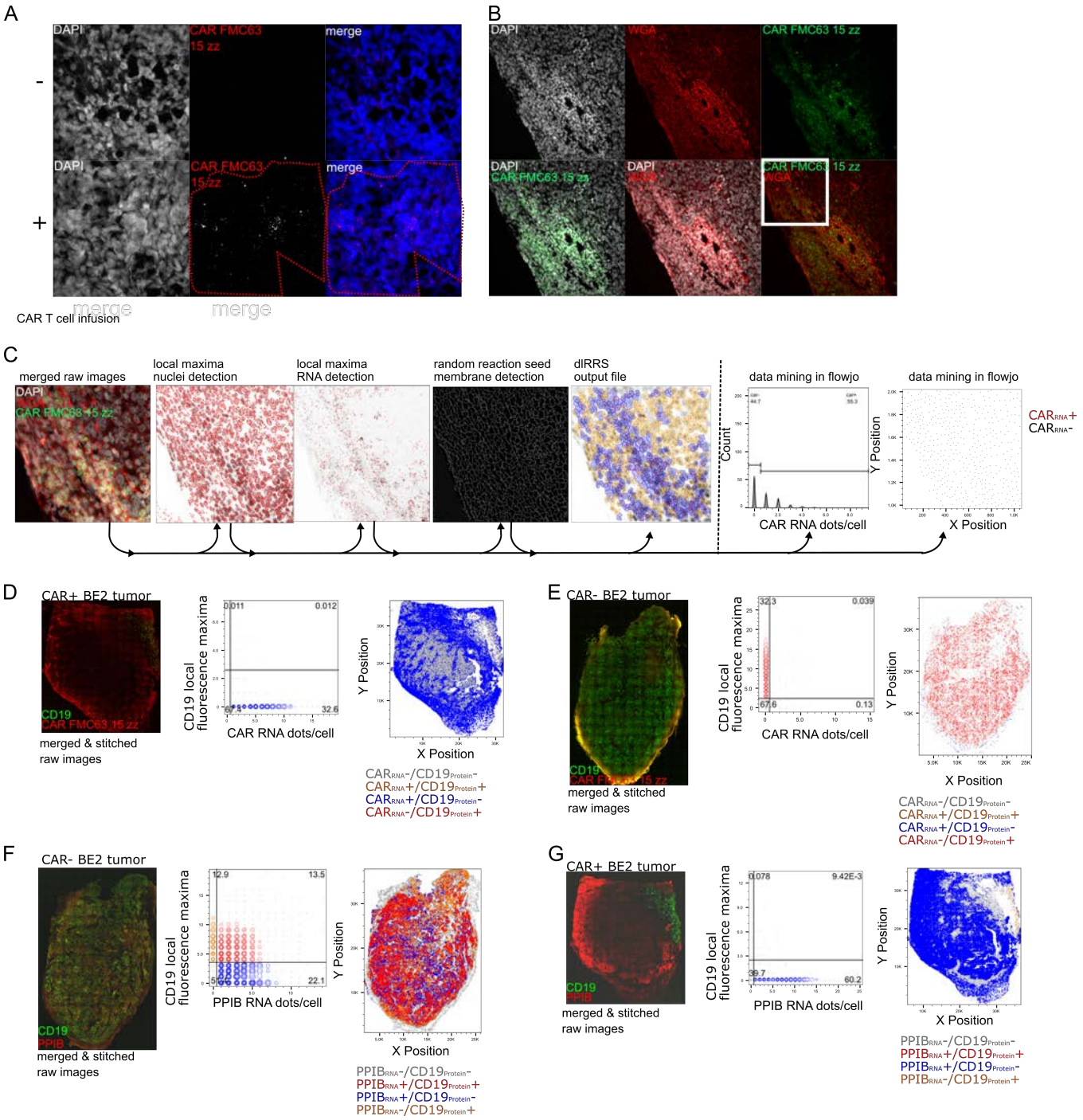
A
DAPI
CAR FMC63 15 zz
merge
-
+
CAR T cell infusion
B
DAPI
WGA
CAR FMC63 15 zz
C
merged raw images
local maxima nuclei detection
local maxima RNA detection
random reaction seed membrane detection
dIRRS output file
data mining in flowjo
Count
CAR RNA dots/cell
Y Position
X Position
CARRNA+
CARRNA-
D
CAR+ BE2 tumor
CD19
merged & stitched raw images
CD19 local fluorescence maxima
CAR RNA dots/cell
Y Position
X Position
CARRNA-/CD19Protein-
CARRNA+/CD19Protein+
CARRNA+/CD19Protein-
CARRNA-/CD19Protein+
E
CAR- BE2 tumor
merged & stitched raw images
CD19 local fluorescence maxima
CAR RNA dots/cell
Y Position
X Position
CARRNA-/CD19Protein-
CARRNA+/CD19Protein+
CARRNA+/CD19Protein-
CARRNA-/CD19Protein+
F
CAR- BE2 tumor
CD19
PPIB
merged & stitched raw images
CD19 local fluorescence maxima
PPIB RNA dots/cell
Y Position
X Position
PPIBRNA-/CD19Protein-
PPIBRNA+/CD19Protein+
PPIBRNA+/CD19Protein-
PPIBRNA-/CD19Protein+
G
CAR+ BE2 tumor
CD19
PPIB
merged & stitched raw images
CD19 local fluorescence maxima
PPIB RNA dots/cell
Y Position
X Position
PPIBRNA-/CD19Protein-
PPIBRNA+/CD19Protein+
PPIBRNA+/CD19Protein-
PPIBRNA-/CD19Protein+

Figure 2

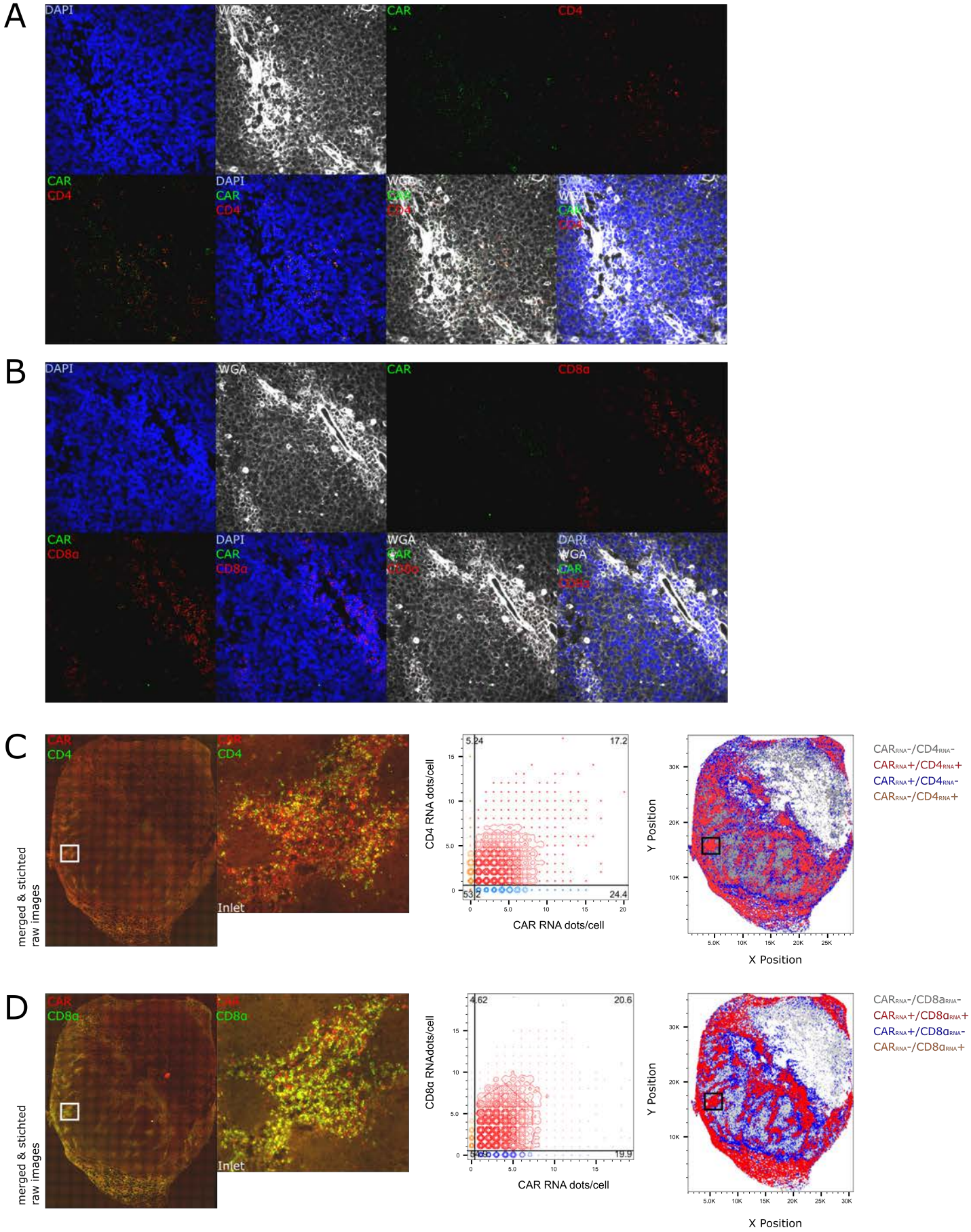
A
DAPI
WGA
CAR
CD4
B
CD8α
C
merged & stichted raw images
Inlet
CD4 RNA dots/cell
CAR RNA dots/cell
Y Position
X Position
CARRNA-/CD4RNA-
CARRNA+/CD4RNA+
CARRNA+/CD4RNA-
CARRNA-/CD4RNA+
D
CD8α RNAdots/cell
CARRNA-/CD8αRNA-
CARRNA+/CD8αRNA+
CARRNA+/CD8αRNA-
CARRNA-/CD8αRNA+

Figure 3

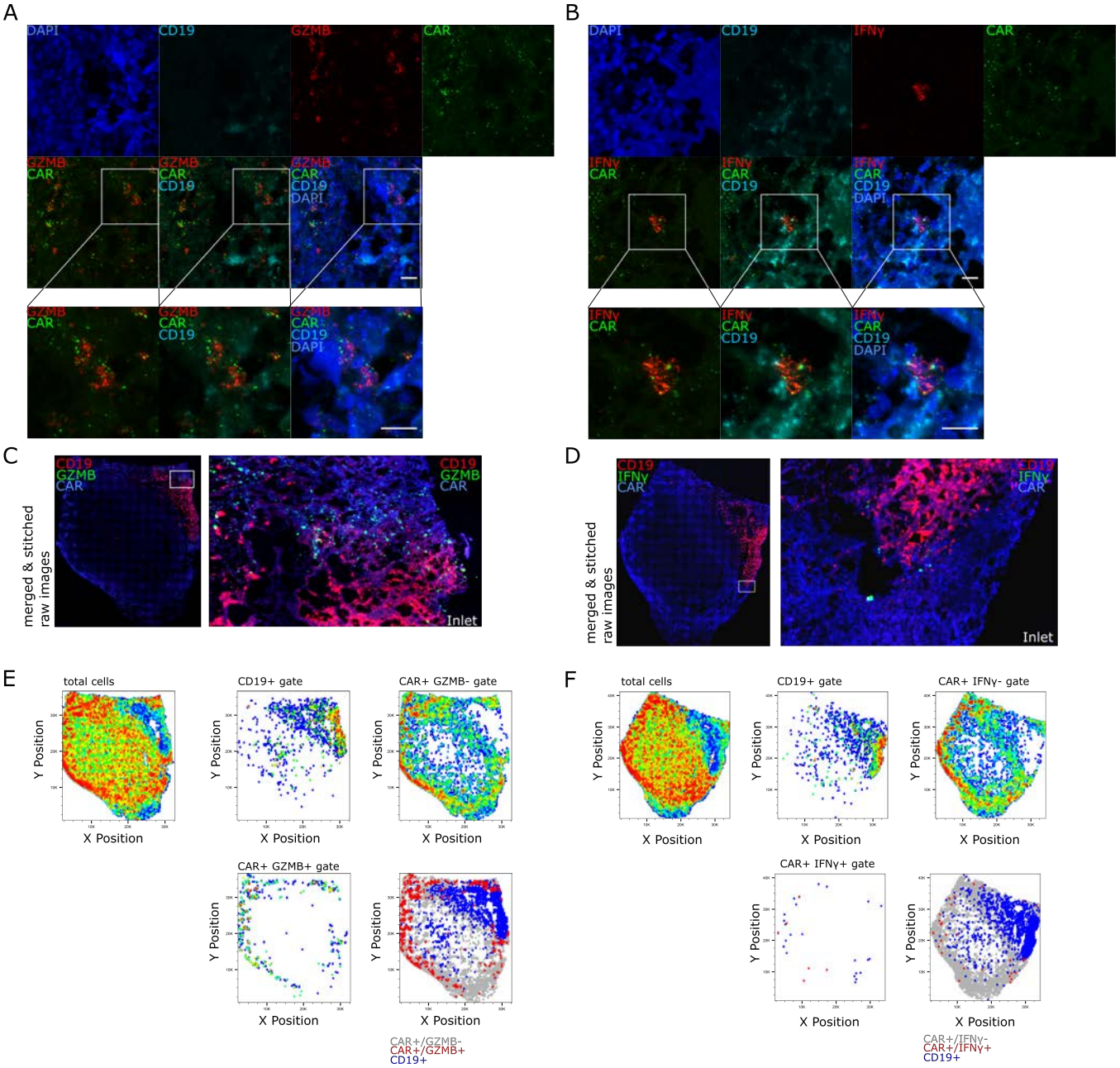
A
DAPI
CD19
GZMB
CAR
GZMB
CAR
GZMB
CAR
CD19
GZMB
CAR
CD19
DAPI
B
DAPI
CD19
IFNγ
CAR
IFNγ
CAR
IFNγ
CAR
CD19
IFNγ
CAR
CD19
DAPI
C
merged & stitched raw images
CD19
GZMB
CAR
Inlet
D
merged & stitched raw images
CD19
IFNγ
CAR
Inlet
E
total cells
CD19+ gate
CAR+ GZMB- gate
CAR+ GZMB+ gate
Y Position
X Position
CAR+/GZMB-
CAR+/GZMB+
CD19+
F
total cells
CD19+ gate
CAR+ IFNγ- gate
CAR+ IFNγ+ gate
Y Position
X Position
CAR+/IFNγ-
CAR+/IFNγ+
CD19+

Figure 4

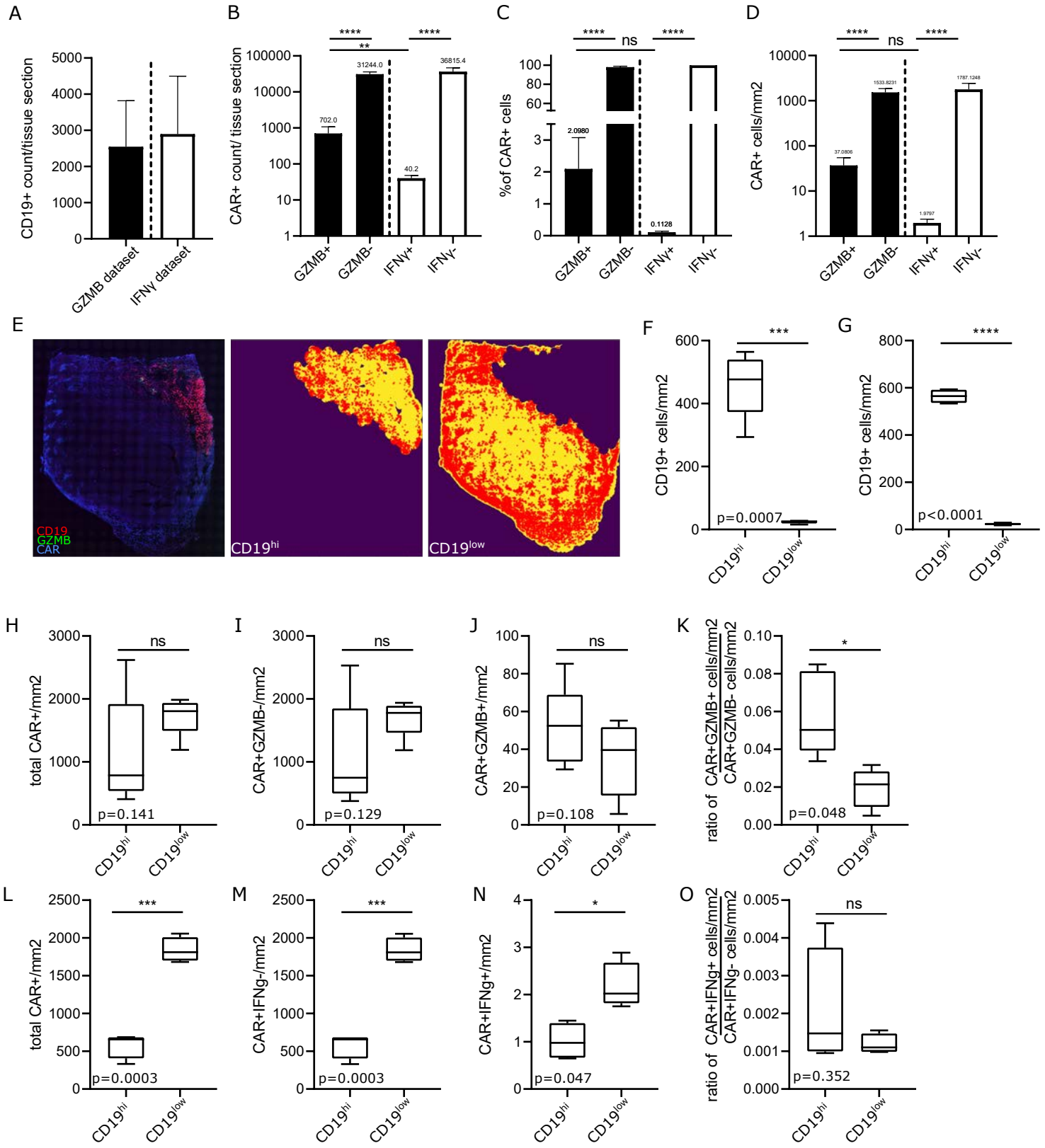
A
CD19+ count/tissue section
GZMB dataset
IFNγ dataset
B
CAR+ count/ tissue section
702.0
31244.0
40.2
36815.4
GZMB+
GZMB-
IFNγ+
IFNγ-
C
%of CAR+ cells
2.0980
0.1128
ns
D
CAR+ cells/mm2
37.0806
1533.8231
1.9797
1787.1248
E
CD19
GZMB
CAR
CD19hi
CD19low
F
CD19+ cells/mm2
p=0.0007
G
p<0.0001
H
total CAR+/mm2
p=0.141
I
CAR+GZMB-/mm2
p=0.129
J
CAR+GZMB+/mm2
p=0.108
K
ratio of CAR+GZMB+ cells/mm2 CAR+GZMB- cells/mm2
p=0.048
L
total CAR+/mm2
p=0.0003
M
CAR+IFNg-/mm2
p=0.0003
N
CAR+IFNg+/mm2
p=0.047
O
ratio of CAR+IFNg+ cells/mm2 CAR+IFNg- cells/mm2
p=0.352

Figure 5

	total zz	scFvCAR core		3'UTR	target tissue/species
FMC63 15zz	15	11	4	0	human and mouse tissue containing different lentiviral constructs
FMC63 27zz	27	11	4	12	human and mouse tissue with only CAR T cells present
FMC63 29zz (JCAR14)	29	11	4	12	human and mouse tissue with only CAR T cells present
VRC07-523 42zz	42	16	13	13	human and nonhuman primate

Supplementary Figure 1

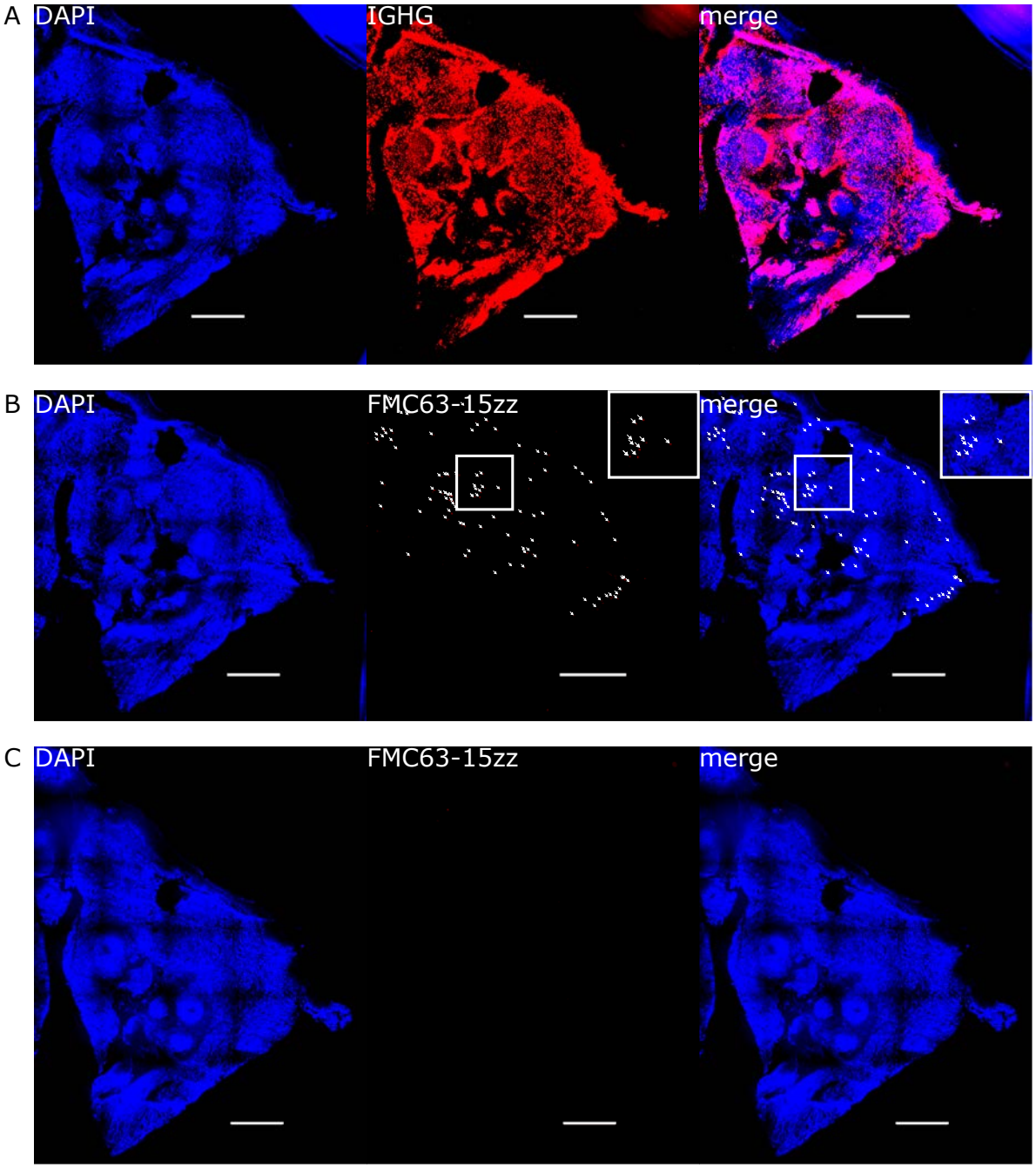

Supplementary Figure 2

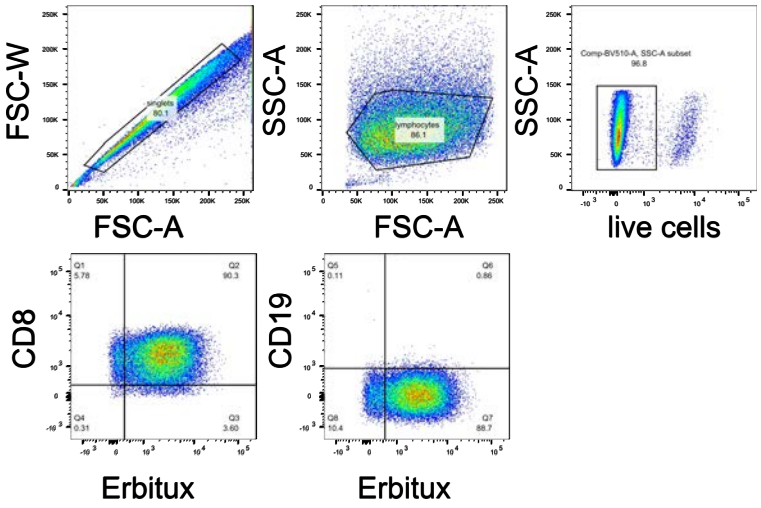

Supplementary Figure 3

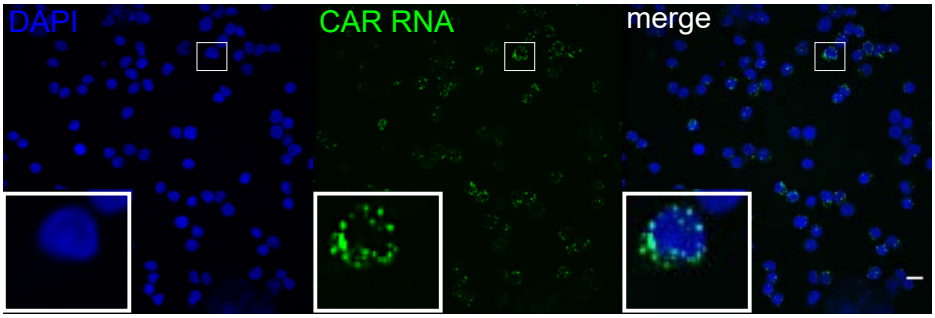

Supplementary Figure 4

A

Jurkat cells

anti-HIV VRC07 CAR Jurkats

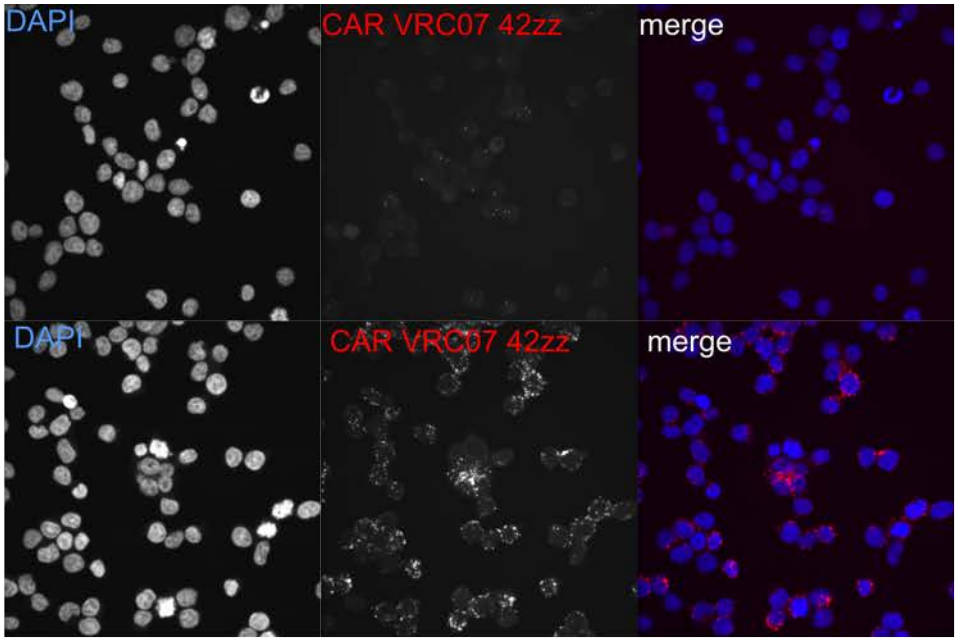

B

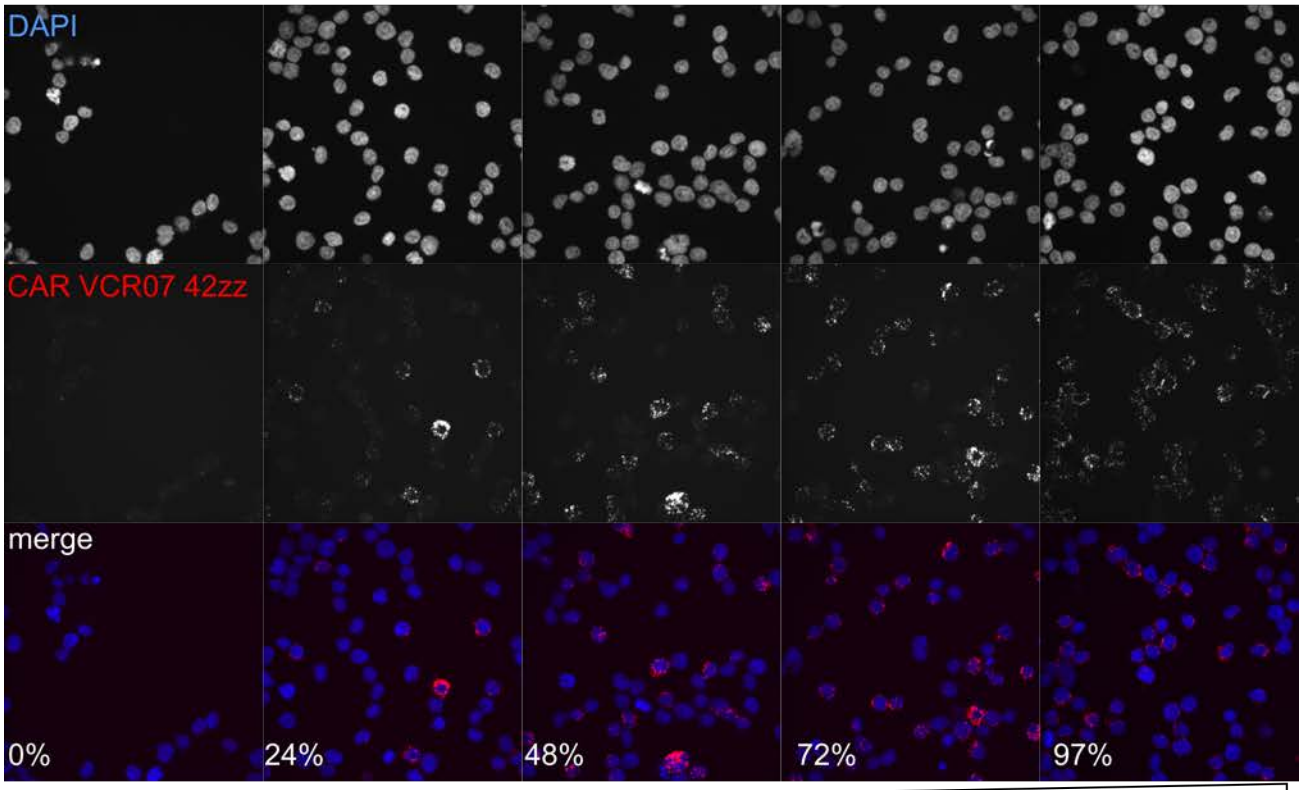

Jurkat cells

anti-HIV CAR Jurkat cells

C

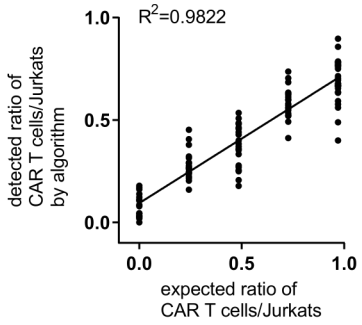

D

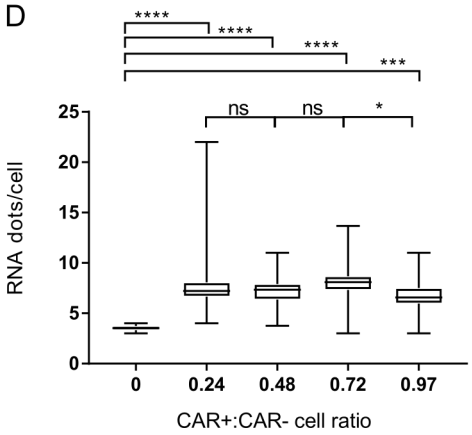

Supplementary Figure 5

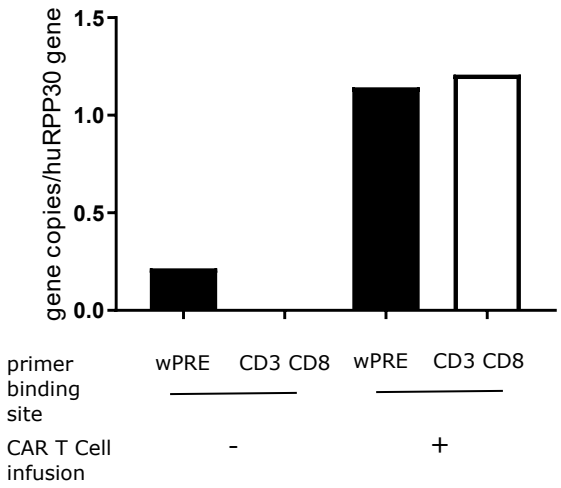

Supplementary Figure 6

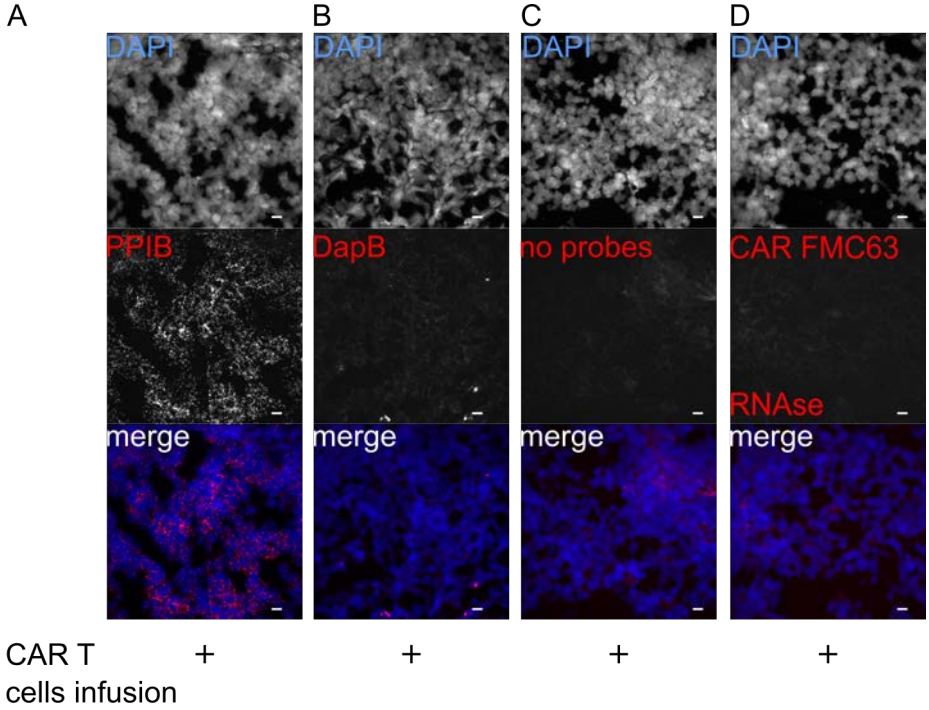

Supplementary Figure 7

A

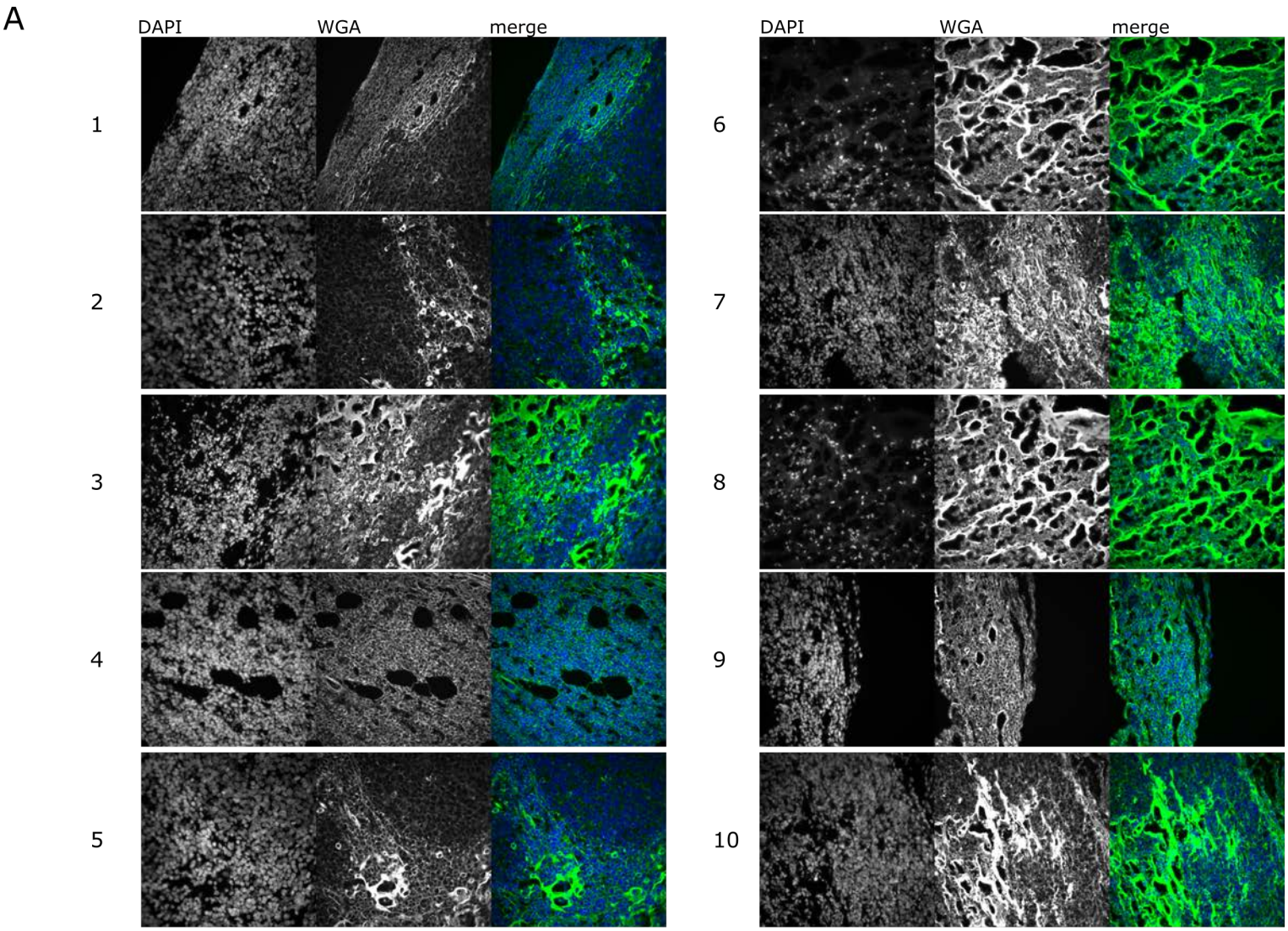

B

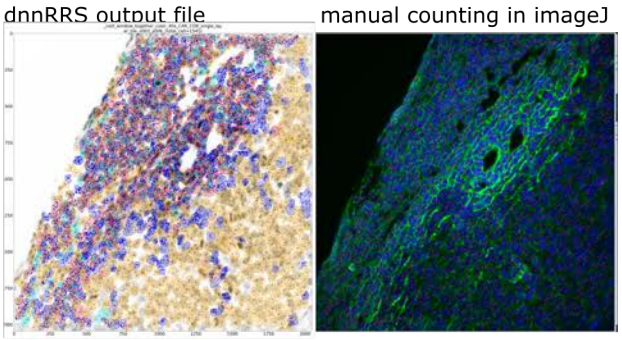

C

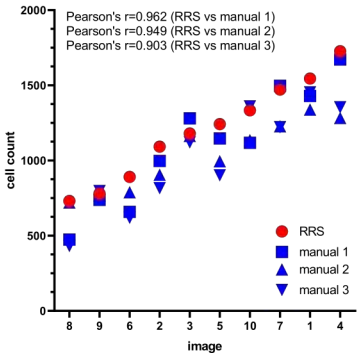

D

image	dnnRRS (h:mm:ss)	manual 1 (h:mm:ss)	manual 2 (h:mm:ss)	manual 3 (h:mm:ss)
1	0:01:41	0:14:50	0:12:26	0:41:19
2	0:01:41	0:08:49	0:07:29	0:28:44
3	0:01:43	0:11:27	0:10:06	0:29:55
4	0:01:27	0:14:56	0:11:25	0:23:34
5	0:01:49	0:10:16	0:09:16	0:13:40
6	0:01:32	0:15:01	0:07:57	0:11:37
7	0:01:38	0:14:02	0:10:47	0:18:37
8	0:00:58	0:10:56	0:07:09	0:25:23
9	0:01:07	0:12:35	0:08:09	0:15:41
10	0:01:06	0:20:46	0:12:45	0:26:03
avergage time/image	0:01:28		0:15:31	
SD	0:00:18		0:08:02	

Supplementary Figure 8

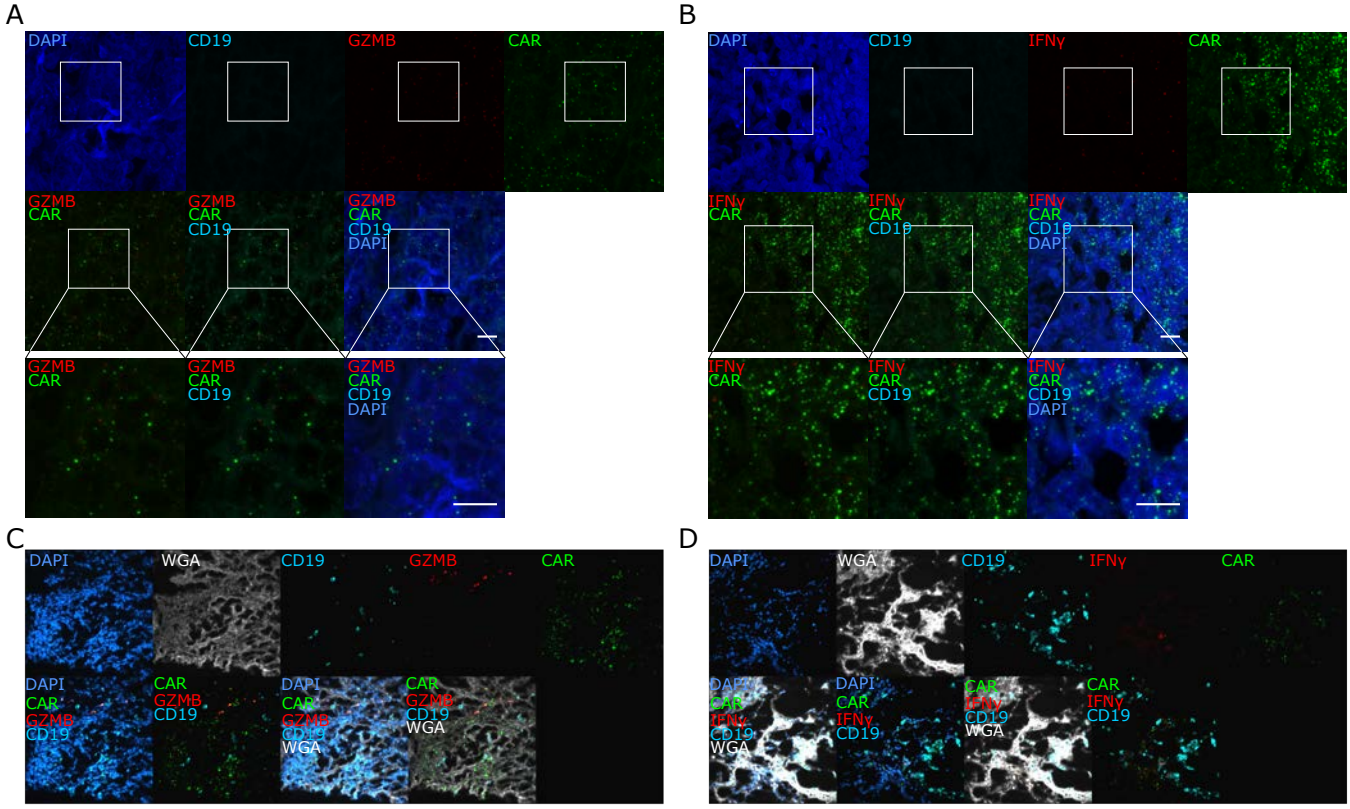

Supplementary Figure 9

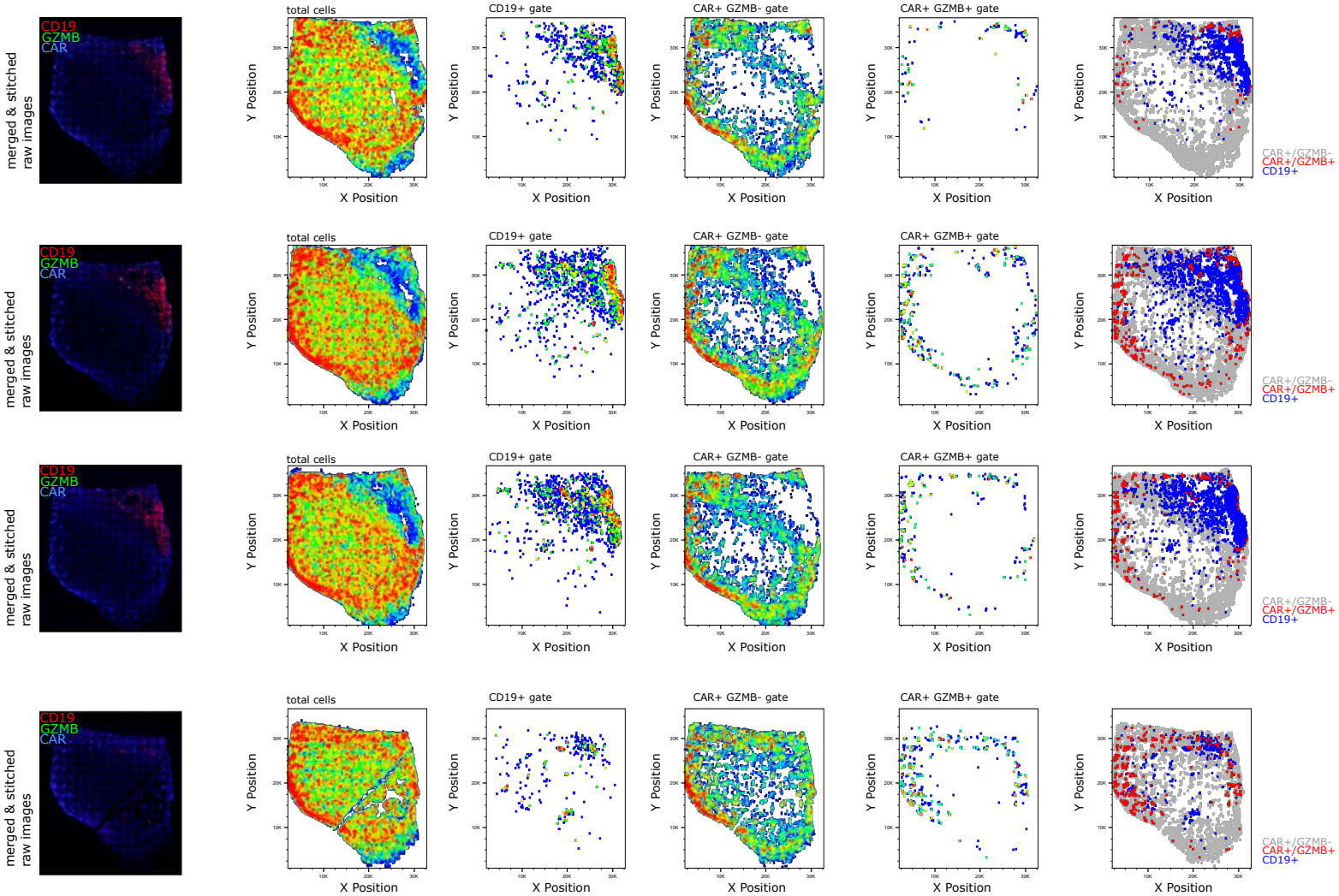

Supplementary Figure 10

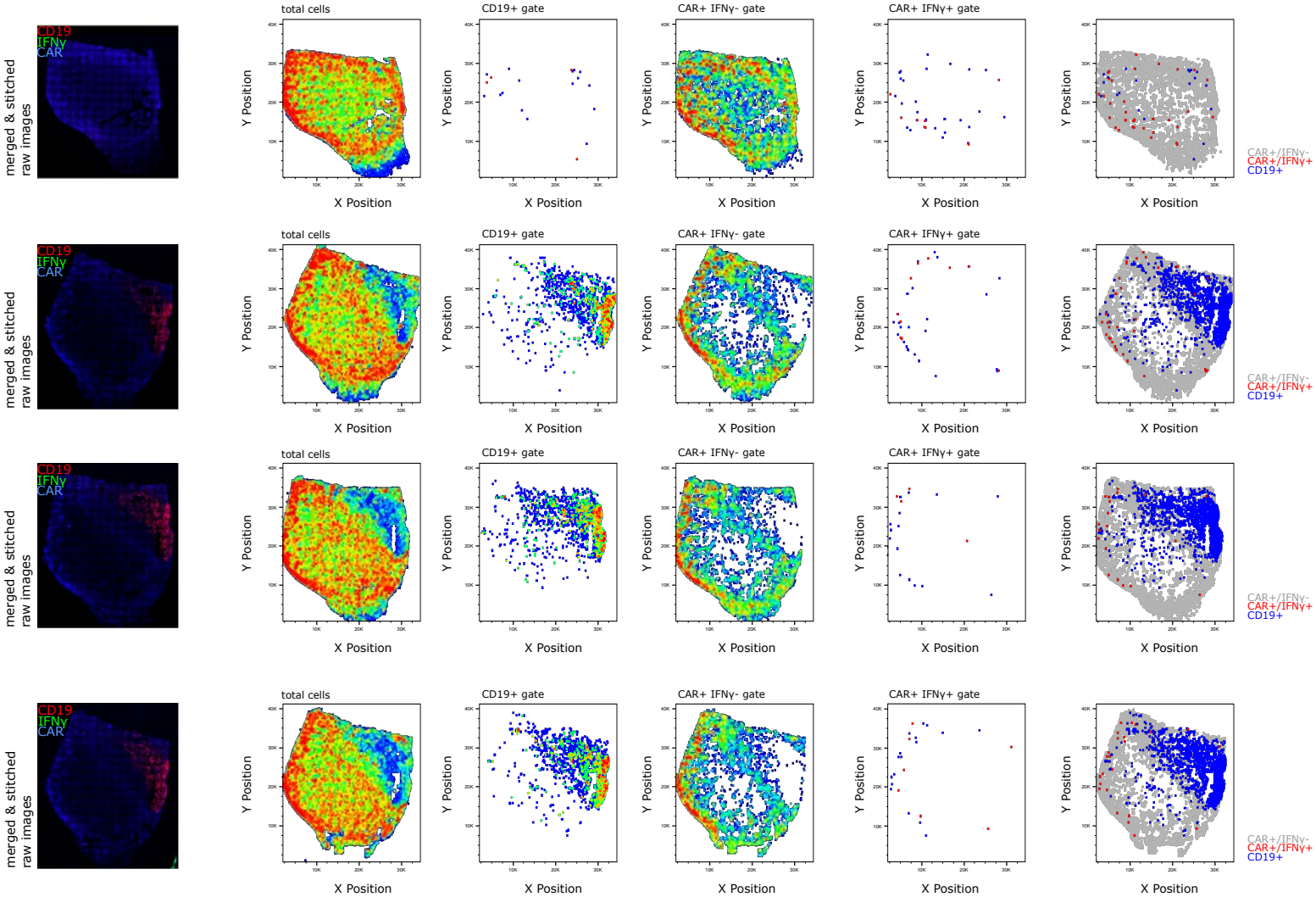

Supplementary Figure 11